Contents lists available at ScienceDirect

Applied Catalysis B: Environmental

journal homepage: www.elsevier.com

K- and Cu-doped $CaTiO_3$-based nanostructured hollow spheres as alternative catalysts to produce fatty acid ethyl esters as potential biodiesel

S. Lanfredi [a, *], J. Matos [b, *], S.R. da Silva [a], E. Djurado [c, d], A.S. Sadouki [e], A. Chouaih [e], P.S. Poon [f], E.R.P. González [a], M.A.L. Nobre [a*]

[a] São Paulo State University (Unesp), School of Technology and Sciences, Presidente Prudente-SP, 19060-900, Brazil
[b] Instituto de Ciencias Químicas Aplicadas, Facultad de Ingeniería, Universidad Autónoma de Chile, 8900000 Santiago, Chile
[c] Université Grenoble Alpes, LEPMI, 1130 rue de la Piscine, F-38402 St Martin d'Hères, France
[d] CNRS, LEPMI, F-38000 Grenoble, France
[e] Laboratory of Technology and Solid Properties (LTPS), Faculty of Sciences and Technology, Abdelhamid Ibn Badis University, Mostaganem, 27000, Algeria
[f] Unidad de Desarrollo Tecnológico (UDT), Universidad de Concepción, Barrio Universitario s/n, Concepción, Chile

ARTICLE INFO

Keywords:
FAEE´s synthesis
$CaTiO_3$-based catalysts
Ultrasonic Spray Pyrolysis
Hollow spheres
K- and Cu-doping

ABSTRACT

New functional polycation oxide-type catalysts were synthesized by the ultrasonic spray-pyrolysis method. The catalytic activity in the production of fatty acid ethyl esters (FAEE´s) using soybean oil was studied. Catalysts are conformed by nanostructured hollow spheres of low density with a stoichiometric formula $Ca_{1-x}K_xTiCu_{x/2}O_3$. The influence of the substitutional ratio (x) upon the catalytic activity was verified. The $Ca_{1-x}K_xTiCu_{x/2}O_3$ sample with x = 0.3 showed the highest activity with a yield up to 89 % to produce fatty acid ethyl esters (FAEE´s) after 24 h reaction using 15 wt.% catalysts, 120 °C and 40 bars. The enhancement in the activity was ascribed to the substitution of the Ca^{+2} sites by K^+ and Ti^{+4} by Cu^{+2} and to the hollow morphology favoring a more effective interaction between the soybean oil and the active basic sites of the catalysts.

1. Introduction

Innovative catalysts can be developed from the concept of an ideal double perovskite structure with $AA'BB'O_6$ or $A_2BB'O_6$. In these materials, the chemical formula exhibits two similar sites called A and A', and two similar sites called B and B' turning feasible in a simultaneous way, a double substitution process in two distinct crystallographic sites of the host structure. This intrinsic feature of the perovskites allows the tailoring its bulk or surface properties. Sites A and A' are preferably occupied by alkaline-earth cations and by alkali metals, respectively. Such structures are quite similar to the classical cubic structure of the perovskite ABO_3 [1], with the difference that the "B" sites in ABO_3 are shared by two cationic species called B and B', which are arranged in alternate way in the three spatial directions [2]. In a preferential way, both B and B' sites are occupied by transition metals [3–7]. The substitution can occur by a great variety of cationic species and even by the same cations with distinct oxidation states. In fact, the physicochemical properties of these compounds including magnetism [8–13], half metallicity and spin polarization [14], multiferroics [15,16] and dielectrics [17] can be engineered or modulated by the correct selection of the type of cation positioned on the B-sites. In this sense, a new class of perovskite-type materials called half-metallic ferromagnets have received an increasing attention in spintronics [18,19]. Such materials have a double property with relation to the electrons spin, they behave like metals in one direction and as semiconductor in another direction.

On the other hand, from a technological point of view, it is even more important to emphasize that the perovskites have been investigated in several catalytic processes such as methane combustion [20], diesel and biodiesel soot combustion [21], dry methane reforming and ethylene homologation reaction [22], and photocatalytic degradation of pollutants in aqueous phase [23–25]. As a general conclusion, the catalytic activity of these oxides is influenced by the type of cation and the site occupied in the structure. Cations on the A sites provide thermal and structural resistance to the catalyst, while cations on the B sites are responsible of the catalytic activity. In addition, the type of A cation and its atomic radii can influence the oxidation state of B cation and the formation of structural defects, respectively, that affect the catalytic activity. For instance, the complex structures of calcium oxides with general formula $CaMO_3$ (M = Ti, Mn, Zr or Fe) [26–27]

* Corresponding authors.
Email addresses: silvania.lanfredi@unesp.br (S. Lanfredi); jmatoslale@gmail.com (J. Matos); marcos.nobre@unesp.br (M.A.L. Nobre)

https://doi.org/10.1016/j.apcatb.2020.118986
Received 27 December 2019; Received in revised form 5 April 2020; Accepted 6 April 2020
Available online xxx
0926-3373/

have shown high catalytic activity in the biodiesel production yielding between 79 - 92% conversion of the oil/alcohol mixture to methyl esters [27]. In addition, a copper-containing calcium titanate, with the stoichiometry formula $CaCu_3Ti_4O_{12}$, has been reported as a multifunctional oxide with an important visible light-driven catalytic activity in environmental remediation [28,29].

In the last years, an increase in the research on the production of biodiesel fuels has been performed [30,31]. The mixture of esters of long chain fatty acids composing biodiesel can be used as an alternative fuel or mixed with diesel or even as fuel in compression-ignition engines [32]. It is well-known this alternative source of energy can reduce the dependence on petroleum-based fuels as well as to reduce the emissions of air pollutants. The biodiesel production is commonly performed by homogeneous catalytic processes using KOH, NaOH and alkoxides as catalysts [33]. However, the product obtained must be neutralized, increasing the operational steps and costs [34]. In this sense, several organic and inorganic heterogeneous basic catalysts such as zeolites, hydrotalcites, anion exchange resins, alkaline earth oxides (CaO, ZnO and MgO), and carbon-based catalysts, have been successfully studied for the production of biodiesel [35,36]. Nevertheless, in the last decades, the nanoparticles have been highlighted as promising catalysts for the biodiesel production due to several properties such as the hierarchical pore size distribution and the high surface area, leading to higher catalytic activity than classical bulk catalysts [22–24]. In addition, these catalysts are suitable for the environmentally friendly biodiesel production [37]. For instance, CaO [38], ZnO [39], Fe (II)-ZnO [40], Ag/ZnO [41], and SiO_2/ZrO_2 [42] nanocatalysts have been used for biodiesel synthesis and several methods have been reported for the synthesis of nanoparticles including ball milling [39], sol-gel [43], sonochemical [44], and microwave irradiation [45]. In addition, sustainable processes for the synthesis of biodiesel have been recently reported iusing Fe_3O_4-PDA-Lipase as surface functionalized nano biocatalysts [46], mixtures of Zn/Mg oxidic nanocatalysts [47], dual-frequency pulsed excited CaO-based catalysts [48], magnetically active and stable cuprospinel $CuFe_2O_4$ catalysts [49], and Cu-impregnated TiO_2 nanocatalysts [50]. However, though these works have reported yields up to 98% in the production of biodiesel, in some cases, the catalysts are expensive and required long and non-eco-friendly synthesis.

All the above-mentioned works have achieved to the general conclusion that the catalytic activity is mainly influenced by the morphology of materials which is highly dependent of the chemical synthesis route. From this point of view, composition and synthesis process should be carefully considered. Alkali-metal containing titanate-based perovskites-like catalysts used for biodiesel synthesis have been prepared by solid-state reactions from a mechanical mixture of carbonate and oxides as starting materials [26,27,51]. However, this route can lead to heterogeneous mixtures. As a general fact, the preparation of $CaTiO_3$ from the mixture of oxides led to the formation of secondary phases as CaO [23]. A complete solid-state reaction requires a number of grinding/regrinding steps of the calcined powders. Nevertheless, intermediate or new metastable phases appear in powders prepared by conventional routes. Otherwise, the methods for the preparation of titanate-based oxide catalysts based on the chemical synthesis tend to improve stoichiometry, surface area and homogeneity [52–55].

In this work, a set of materials based on the $CaTiO_3$ host structure were synthesized by spray pyrolysis method. This method allowed to prepare nanostructured hollow spheres with a high chemical and structural reproducibility. These materials, with the formula $Ca_{1-x}K_xTiCu_{x/2}O_3$ where x = 0, 0.2 and 0.3, were studied as promising heterogeneous catalysts in the transesterification reaction for the production of fatty acid ethyl esters (FAEE´s) by the ethylic route as potential biodiesel fuel. The influence of temperature, pressure, reaction time and catalyst concentration upon the catalytic activity was verified and discussed in terms of the physicochemical properties of the materials.

2. Experimental

2.1. Synthesis and Characterization of doped $CaTiO_3$

Hollow particles constituted by a single-phase solid solution described by the general formula $Ca_{1-x}K_xCu_{x/2}TiO_3$, were synthesized by the spray-pyrolysis method [56–59]. The materials $CaTiO_3$, $Ca_{0.8}K_{0.2}Cu_{0.10}TiO_3$, and $Ca_{0.7}K_{0.3}Cu_{0.15}TiO_3$ were denoted as CT, CaKCT-0.2 and CaKCT-0.3 for x = 0, 0.2 and 0.3, respectively. This chemical route of synthesis allowed the preparation of nanostructured materials with a narrow particle size distribution and a high reproducibility [60,61]. Prior to the aerosol formation, precursor solutions of CT, CaKCT-0.2 and CaKCT-0.3 were prepared using titanium isopropoxide ($Ti([OCH(CH_3)_2]_4$, 97% Aldrich), citric acid ($C_6H_8O_7.H_2O$, 99.5% Nuclear), potassium nitrate (KNO_3, 99.0% ReAgen UK), copper nitrate ($Cu(NO_3)_2$, 99.0% ReAgen UK) and calcium nitrate ($Ca(NO_3)_2.4H_2O$, 99.0% ReAgen UK) as starting reagents. An aqueous solution (250 mL) was prepared mixing citric acid and titanium isopropoxide at 70 °C in a molar ratio 3:1. Citric acid avoids the ultrafast hydrolysis of $Ti[OCH(CH_3)_2]_4$. Two different concentrations of the solutions with these precursors were investigated, 0.025 mol L^{-1} and 0.1 mol L^{-1}. Solutions were ultrasonicated in a high frequency ultrasonic generator operating at 1.7 MHz. The aerosol was conducted from the ultrasound apparatus to the reactor within a tubular furnace, using a mixture of nitrogen and oxygen as carrier gas with a flow rate of 3 L min^{-1}. The temperature was set at 750 °C and 850 °C prior to reach a complete pyrolysis with the subsequent formation of the oxide.

The morphology of powders was verified by scanning and transmission electron microscopy (SEM/TEM). SEM analysis was performed using a microscope model Curls Zeiss EVO LS15, operating at 30 kV. Samples were coated with a thin gold film by the evaporation method. Quantitative analysis of SEM images was derived from a statistical image processing using the ImageJ program. TEM characterization was performed in the Microscope, Jeol, JEM-2100, equipped with EDS, Thermo scientific, operating at 200 kV. All samples were dispersed in ethanol (99.98%), using an ultrasonic cleaner during 15 min. Then, an aliquot of the sample was deposited on the carbon-coated copper screen. After drying, samples were characterized.

Textural properties were obtained from the N_2 adsorption/desorption isotherms at −196 °C using an Autosorb iQ Station 2 apparatus. Surface area was determined by BET (Brunauer–Emmett–Teller) equation, while BJH (Barrett–Joyner–Halenda) method was used to obtain the total volume of pores and the average pore diameter.

The active sites of the catalysts surface were determined by the Hammett indicator method [62] using methyl orange (pKa = 3.3), neutral red (pKa = 6.8), thymol blue (pKa = 8.8), phenolphthalein (pKa = 9.8) and alizarin yellow (pKa = 11.1). The quantitative determination of basicity was done by titration with benzoic acid. A suspension of 0.15 g of catalyst in methanolic solution of indicator (2 mL, 0.1 mg mL^{-1}) was stirred for 30 min and then titrated with a methanolic solution of benzoic acid (0.01 mol L^{-1}). The experiments were performed by adding the indicator solution to a suspension of the catalyst and the change of color was observed upon adsorption of the indicator on the surface of the catalyst, as a result of a contribution of all acidic and basic sites in the catalyst. An indicator with a higher pKa is deprotonated only upon reaction with stronger basic sites. When the number of deprotonated molecules is higher than protonated molecules, the basic color is observed. In this work a change in the color of the suspension was only observed at high pKa, indicating the presence of basic sites for all catalysts prepared.

Chemical bonds of catalysts were studied by Fourier transformed infrared spectroscopy (FTIR) in the range from 4000 to 400 cm^{-1} in a Shimadzu spectrometer (model IRAffinity-1).

Structural features of $Ca_{1-x}K_xCu_{x/2}TiO_3$ powders with x = 0, 0.2 and 0.3 were obtained by X-ray diffraction (XRD) patterns using a Shimadzu diffractometer (model XRD-6000) with Cu-Kα_1 radiation and a graphite monochromator. Data were collected between $5^\circ \leq 2\theta \leq 80^\circ$ with a scanning step of 0.02° and a fixed counting time of 10 s. The crystallite size (D) was calculated by Scherrer's equation with the use of the Jade 8 Plus software [63]. The crystallinity index of powders was obtained using the Eq. (1) where I_o^{112} is the maximum intensity associated to the diffraction line (112) of the crystallographic plane for calcium titanate 100% crystalline and I^{112} is the maximum intensity related to the (112) diffraction line of the powders.

$$\text{Crystallinity index (\%)} = (I^{112}/I_o^{112}) \times 100 \quad (1)$$

Crystalline structures were refined by the Rietveld method using the Fullprof program [64,65]. Functions used for the background level and peak shape were polynomial 5-order and pseudo-Voigt, respectively. The diffraction line full-width at half-maximum FWHM (*H*) was determined by the Caglioti function [66]. The crystalline structures were built using the Diamond software®.

2.2. Catalytic tests: Fatty acid ethyl esters synthesis

The transesterification reaction for the synthesis of fatty acid ethyl esters (FAEE´s) was carried out in a Parr autoclave reactor. High-quality soybean oil was the feedstock used in the present work. The acid value of the feedstock is one of the most important characteristcs of a feedstock to be used for the biodiesel synthesis. The acid value of the present soybean oil was equal to 0.015 mg g^{-1}. The acidity index value was determined using 1 g of refined soybean oil diluted with 50 mL of ethyl alcohol in a 125 mL Erlenmeyer with mild heating and stirring. After this, 0.05 mol L^{-1} of KOH solution was dropped using a burette into the ethanolic soybean solution containing phenolphthalein as indicator until complete disappearance of the pink color of the medium. The acidity index (AI) is a measure of the amount of free fatty acids in the oil. This parameter was estimated by the Eq. (2), where V is the volume of KOH used for neutralization (mL), C_{KOH} is the concentration of the KOH solution (mol L^{-1}), 56 is the molecular weight of KOH (g mol^{-1}), and m is the weight of the soybean oil sample (g).

$$IA = (V\ C_{KOH}\ 56)/m \quad (2)$$

Additional data of the physicochemical characteristics of the soybean oil used as feedstock in the present work, including the saponification value, density and refraction index are shown in the Table S1 (supplementary material). It can be seen these values are within the respective ranges reported by the Brazilian legislation to qualify the soybean oil.

For the catalytic tests, 100 mL mixture containing ethanol and soybean oil in the molar relation 40:1 was poured into the reaction vessel and the solid catalyst was added using, 5, 10 and 15% *wt.* related to the soybean oil weight. The reaction was followed from 8 - 24 h, using temperatures between 60 - 120 °C and N_2 pressures of 1 - 40 bar. The mechanical stirring was constant ca. 600 rpm in all the catalytic tests. In preliminary studies [67] the optimization of the experimental conditions to obtain the highest yield of FAEE´s has been described. These conditions are the following. Molar ratio ethanol/soybean oil 40:1, pressure 40 bar pressure and 120 °C as temperature of reaction. The experimental conditions used in the present work are within the range reported in most of recent works of biodiesel production. For instance, catalysts concentration from 1 wt.% [46] up to 20 wt.% [50]; temperature from 30 [46] up to 80 °C [50], reaction times between few minutes [48] up to 48 h [46]; alcohol:oil ratio from 3:1 [46] up to 30:1 [50]. After the catalytic tests, the heating and the stirring were stopped, and the reaction vessel was permitted to cool down following the depressurization of the reactor. Then, the catalyst was removed by centrifugation process of the organic solution [67] and the resulting solution was filtrated to obtain the mixture of FAEE´s. The FAEE´s composition was analyzed by gas chromatography with a flame ionization detector (GC-FID) and GC-coupled mass spectroscopy (MS-GC). The GC-FID analysis was carried out using a Shimadzu apparatus, model GC-2010. A capillary Rtx-Wax column (30 m x 0.25 mm x 0.25 mm thickness) was used. A progressive temperature program was performed to optimize the GC-FID analysis. The injector and detector were maintained at 250 °C. The carrier gas flow (N_2) was ca. 1 mL min^{-1} with a linear velocity ca. 23.4 cm s^{-1}. The injection mode was 1:15 split less and the injection volume of samples was 1 μL. The identification and quantification of the compounds were accomplished by the injection of a standard of ethyl oleate (5 at 50 mmol/L) and the yield of FAEE´s was calculated with a standard curve as described elsewhere [68–70]. All analyses were done by triplicate.

The yield of FAEE´s (FAEE Yield) was calculated in terms of the conversion of the soybean oil using the Eq. (3), where EO is the concentration of ethyl oleate, F is a dilution factor, MW is the molecular weight of the oil, and P is the experimental percentage of ethyl oleate.

$$\text{FAEE Yield (\%)} = \{[(EO).(F)]/[(\text{weight})/(MW) \times 3 \times P)]\}.100 \quad (3)$$

Additional consecutive catalytic runs were performed to verify the reuse of catalysts. After each consecutive catalytic run, the leaching of metals from catalysts was verified. To do this, the solution with the transesterification mixture was filtrated and washed with hexane (10 mL) after the catalytic test, and traces of metals, mainly K and Ca were verified by flame atomic absorption spectrometry (FAAS) technique, with a continuous source lamp and current of 13 A. The analysis was performed according to the Brazilian Standard Method ABNT NBR 15556. The instrumental parameters for K determination were: λ = 766.4908 nm; burner height = 8 mm; gas flow = 60 L h^{-1}; C_2H_2/air = 0.130, while for Ca were: λ = 422.6728 nm; burner height = 13 mm; gas flow = 40 L h^{-1}; C_2H_2/air = 0.100.

Table 1
Textural properties obtained from the N_2 adsorption/desorption isotherms at −196 °C for the CT, CaKCT-0.2 and CaKCT-0.3 samples prepared at 850 °C from 0.1 mol L^{-1} of precursor solution.

Samples	S_{BET} ($m^2 g^{-1}$)	V_{micro} ($cm^3 g^{-1}$)	V_{meso} ($cm^3 g^{-1}$)	V_{meso}/V_{tot} (%)	V_{total} ($cm^3 g^{-1}$)	W (nm)
CT	54	0.016	0.230	93	0.246	5
CaKCT-0.2	52	0.012	0.292	96	0.304	10
CaKCT-0.3	44	0.008	0.221	97	0.229	13

3. Results and Discussion

3.1. Characterization of the materials

3.1.1. Morphology: SEM and TEM studies

Fig. 1 shows the SEM micrographs for CT, CaKCT-0.2 and CaKCT-0.3 samples obtained at 850 °C from 0.1 mol L^{-1} of precursor solution. The morphology of all the materials is spherical and the samples are characterized by a high degree of roughness. It can be seen from the magnification of the SEM images for CaKCT-0.2 (inset, Fig. 1b) and CaKCT-0.3 (inset, Fig. 1c), that the present particles are hollow spheres indicating a low density of these materials. This characteristic can be associated with the solvent evaporation rate [71]. The drip increases with the increase of the concentration of the precursor solution and a fast evaporation of the solvent can induce to the formation of a salt crust on the surface of the particles, prior to the pyrolysis [72].

The histograms associated to the particle size distribution (Fig. 1) showed that CaKCT-0.2 developed a similar particle size distribution to that observed on the CT sample, with a maximum size of particle

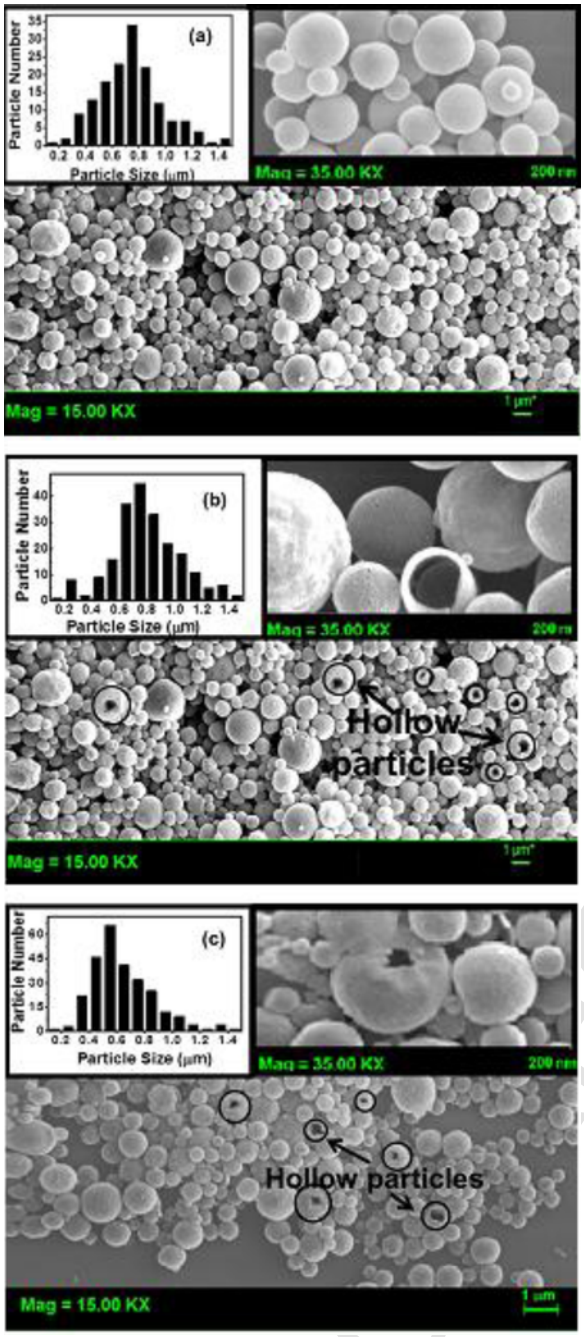

Fig. 1. SEM images for the samples prepared at 850 °C from 0.1 mol L^{-1} of precursor solution. (a) CT. (b) CaKCT-0.2. (c) CaKCT-0.3.

ca. 700 nm. By contrast, CaKCT-0.3 sample is characterized by a maximum size of ca. 500 nm. It could be due to higher cohesion forces between the spherical particles promoted by a higher copper content. The ionic radii of Cu^{+2} is clearly lower than that of Ca^{+2} (0.73 Å against 1.00 Å), and during the coalescence mechanism [73] a higher cohesion between the spheres could be responsible of the formation of particles with smaller sizes. For the lowest concentration of precursor solution (0.025 mol L^{-1}), the CT powders also presented particles with spherical shape but with a smoother surface as shown in **Figure S1** (**supplementary information**). As a general fact, the lower concentration of the precursor solution yields smaller and less agglomerated particles with an average size between 200 and 500 nm, than using 0.1 mol L^{-1} of precursor solution (Fig. 1a**)**. Similar results were observed for the CaKCT-0.2 and CaKCT-0.3 samples (**Figure S2** and **S3**, respectively, **Supplementary**). It must be point out that fractures in the shells of the CaKCT-0.2 and CaKCT-0.3 spheres prepared from the diluted precursor solution were not detected (**Figure S1, Supplementary**). This result suggests that sintering effect is not taking place in these samples or that thickness of wall particles is large enough to prevent the fracture. As noted above, the spheres were formed by a coalescence phenomenon between particles of similar size [73]. This is a clear evidence that the present materials are nanostructured. This aspect can also be further visualized in the SEM images shown in **Figure S3** (**Supplementary)** for the CaKCT-0.3 sample where the average particles size range between 400 – 800 nm.

The increase in the substitutional ratio (x) led to a change in the surface of the particles. For instance, CaKCT-0.2 and CaKCT-0.3 samples (Fig. 1), are constituted by hollow spheres when a high concentration of precursor solution is used (0.1 mol L^{-1}). The particles showed more roughness on the surface of CaKCT-0.3 sample. In addition, this sample also shows an important presence of salt crust on the surface before the pyrolysis. This phenomenon suggests that stoichiometry of the precursor solution play an important role in the control of the particle surface as can be visualized in the TEM images (Fig. 2**)** for CT, CaKCT-0.2 and CaKCT-0.3 samples prepared at 850 °C from 0.1 mol L^{-1} of precursor solution.

The higher the ratio x, the higher the fraction of particles with larger sizes, that after the crystallization, tend to agglomerate and growth forming spheres with multiple grains/crystals. It should also be mention that the evaporation of the solvent may changes the concentration of precursor salt, leading to a saturation of the concentration in the solution of the precursor. As consequence, a precipitation of the precursor on the drip surface occurs [74], since the solvent evaporation is more rapid than its diffusion, which is clearly affected by the saturation of the solution. This feature results in a porous hollow particle, as well as an increase in the roughness degree of the particles, in agreement with the features observed in the SEM (Fig. 1c) and TEM images (Fig. 2c). In this way, the concentration of the precursor solution has an important role on both spherical form and roughness of particle. As expected, the crystalline plane indexed in the TEM images were (111) and (021), were both associated with the host structure $CaTiO_3$ having orthorhombic symmetry as can be seen from Fig. 2.

3.1.2. Textural properties: N2 adsorption/desorption isotherms

It is well-known that biodiesel is composed by esters of long-chain fatty acids with a large molecular size containing single chains of 12 to 24 carbon atoms [75]. Thus, textural properties are important characteristics of the materials since these parameters have a significant role on the catalytic activity for the biodiesel production. **Figure S4** (**Appendix**) shows the N_2 adsorption–desorption isotherms at −196 °C obtained for the samples prepared at 850 °C from a concentration of 0.1 mol L^{-1} of the precursor solution. A summary of the main textural parameters such as surface area (S_{BET}), total volume of pores (V_{total}), volume of micropores (V_{micro}), volume of mesopores (V_{meso}), and the most probably pore diameter (W), of the CT, CaKCT-0.2 and CaKCT-0.3 samples are listed in the Table 1. It can be seen from **Figure S4** that all materials showed IV-type isotherms and H3-type hysteresis loops according to the new classification of physisorption isotherms and hysteresis loops [76]. This type of isotherm corresponds to materials with a framework mainly composed by mesopores in the range 2 - 50 nm, with a small contribution of micropores. The adsorption behavior in mesopores is determined by the adsorbent-adsorptive interactions and by the molecular interactions in the condensed state [76]. This type of hysteresis can be given by non-rigid particles such as the present nanostructured spheres but also, they occur if the pore framework consists of macropores which are not filled with pore condensate [76].

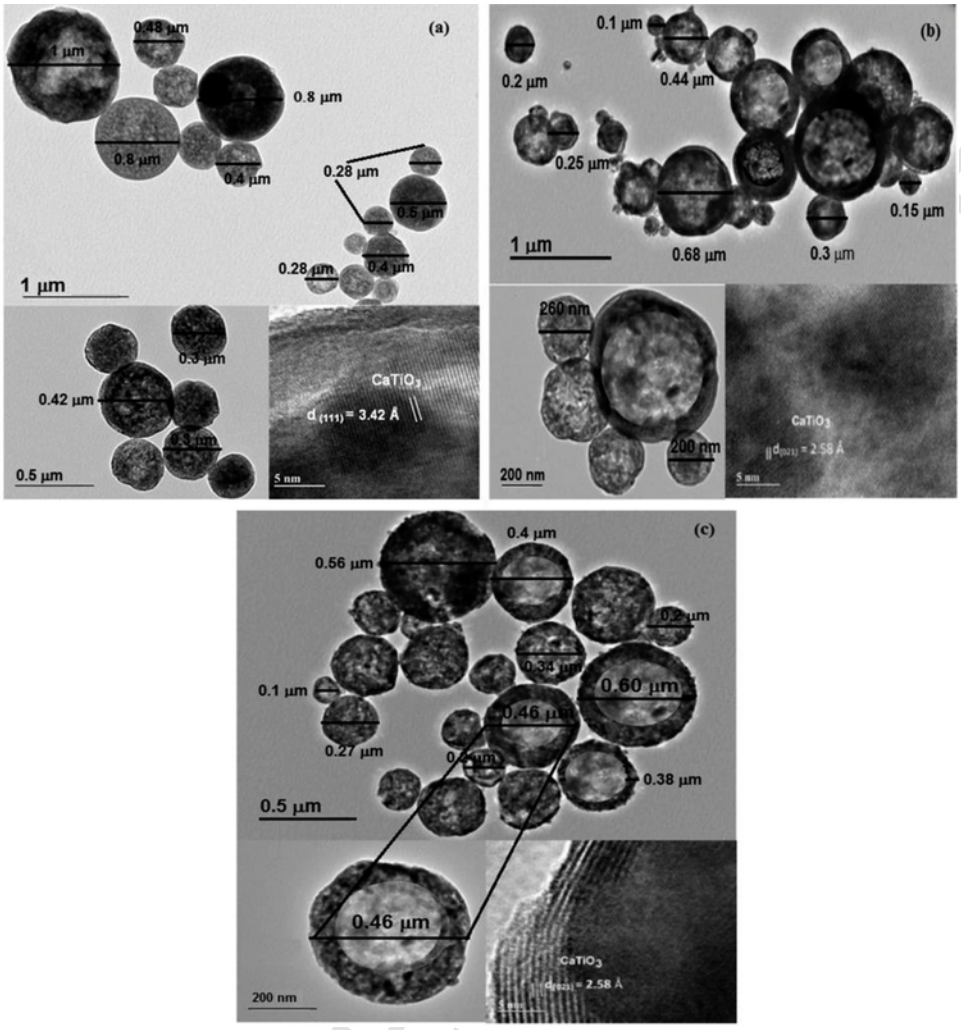

Fig. 2. TEM images of the samples prepared at 850 °C from 0.1 mol L^{-1} of precursor solution. (a) CT. (b) CaKCT-0.2. (c) CaKCT-0.3.

It is interesting to note that the hysteresis branch for the desorption are remarkably narrowed for the CaKCT-x powders, where x = 0.2 and 0.3. This can be associated with the hollow spaces in the spheres prepared with a high value of x ratio, yielding to fractures of the materials. Consequently, a decrease in the surface area from 54 $m^2 g^{-1}$ to 44 $m^2 g^{-1}$ is observed (Table 1). In addition, it is interesting to note the influence of the x ratio upon the pore size distribution (PSD) of the materials. Fig. 3 shows the PSD (Figs. 3a**, 3c** and **3e**) of the samples in terms of the differential change of pore volume and the cumulative pore volume as a function of the mean pore diameter. The PSD became broader with the increase in the x ratio. Accordingly, the most probably pore diameter increased from 5 to 13 nm, following the order: CT < CaKCT-0.2 < CaKCT-0.3. In consequence, the contribution of mesopores to the total volume of pores increased (Table 1), mainly for the large mesopores (diameter > 100 Å). The contribution of pores with diameter > 100 Å was calculated from data in Figs. 3b**, 3d** and **3f**. These values are ca. 47 %, 68 % and 72 % for CT, CaKCT-0.2, and CaKCT-0.3, respectively. Thus, it can be concluded that the changes observed from the textural properties (Fig. 3) agree with the changes in morphology discussed above from the TEM images (Fig. 2).

3.1.3. Chemical Bond analysis: FTIR spectroscopy

Fig. 4 shows the FTIR spectra of the samples obtained at 850 °C from the precursor solution with ca. 0.1 mol L^{-1} concentration. The transmittance FTIR spectra shows major absorption bands below 1000 cm^{-1} positioned at 670 cm^{-1}, 582 cm^{-1}, 563 cm^{-1} and 438 cm^{-1} that can be attributed to titanate-based materials. These bands can be assigned to the titanium cation related to the stretching vibration of Ti–O between 670–550 cm^{-1} and Ti–O–Ti at 438 cm^{-1} [77,78]. A shift to higher wavenumbers for the Ti-O stretching vibration is observed from CT to CaKCT-0.3 powders. The replacement of Ca by K and Cu cations positioned on the A-site of the CT host structure cations yields a shift of the Ti-O stretching from 563 cm^{-1} in the CT to 582 cm^{-1} in CaKCT-0.2 and CaKCT-0.3. These bands have been assigned to the vibration mode stretching-type related to the Ti-O bond length [79]. The shift observed to higher wavenumbers indicates an increase in the strength of the Ti-O bond.

The absorption band at 438 cm^{-1} is characteristic of the bending mode and it is related to changes in the bond angle associated to Ti-O-Ti. Both Ti–O and Ti-O-Ti bands are assigned to the [TiO_6] octahedra in the perovskite structure [80]. These FTIR findings can be related to an increase in the ionic character of the Ti-O bond. The bands observed at 1530 cm^{-1}, 1389 cm^{-1}, and 1274 cm^{-1} can be attributed to vibrational modes of the carbonate group CO_3^{2-} [81]. As expected, all the samples showed similar peaks at 3446 cm^{-1} and 1657 cm^{-1} assigned to O-H stretching and bending modes of water molecules.

3.1.4. Structural analysis: X-ray diffraction

Fig. 5 shows the XRD pattern of the samples obtained at 750 °C and 850 °C as a function of the precursor solution concentration. All sam-

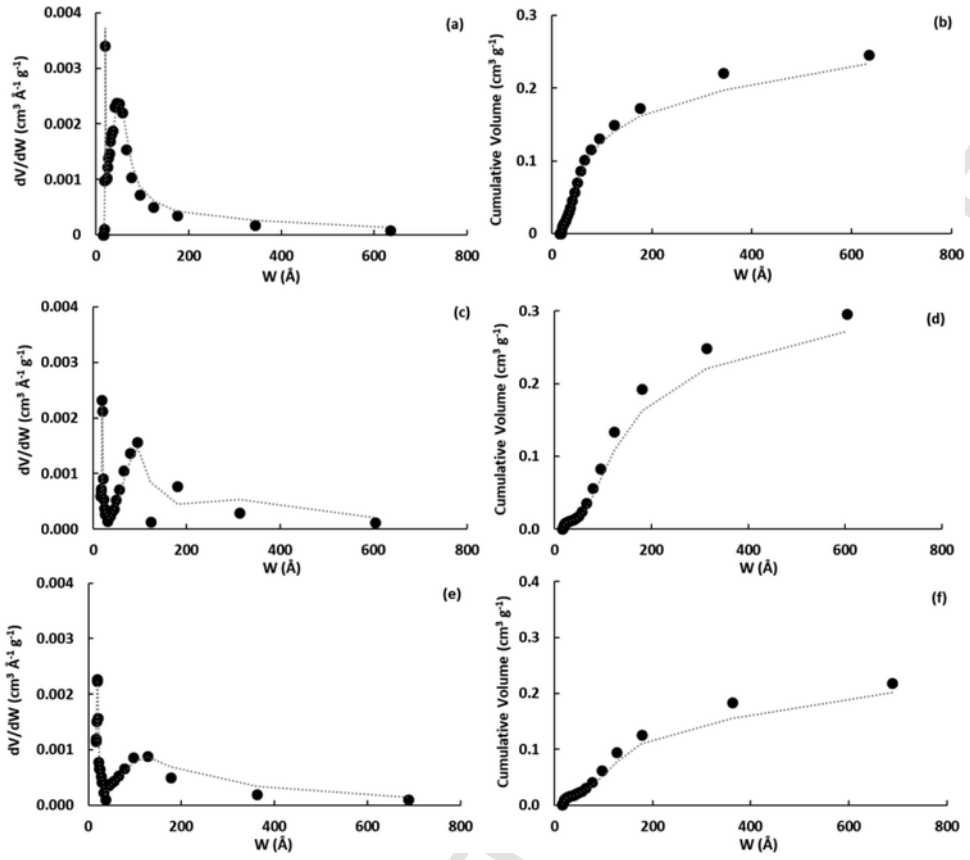

Fig. 3. Pore size distributions (Figures a,c,e) and cumulative pore volume (Figures b,d,f). (a-b): CT. (c-d): CaKCT-0.2. (e-f): CaKCT-0.3.

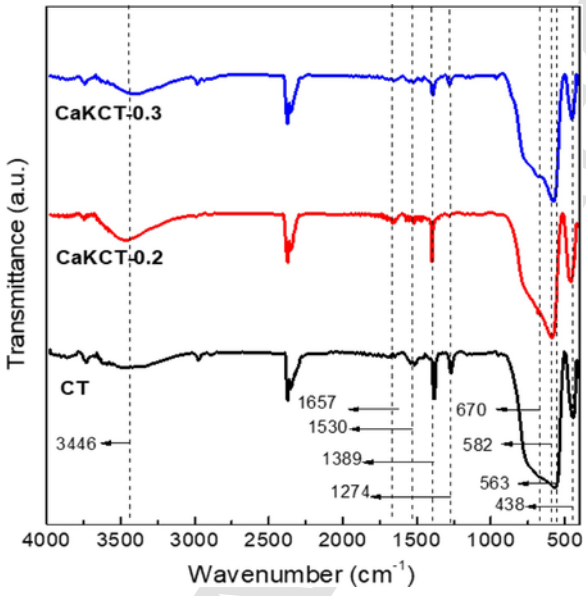

Fig. 4. FTIR transmittance spectrum of CT, CaKCT-0.2 and CaKCT-0.3 samples obtained at 850 °C from 0.1 mol L^{-1} of precursor solution.

ples exhibited a set of diffraction lines ascribed to $CaTiO_3$ with orthorhombic symmetry and space groups Pbnm (JCPDS card number 78-1013).

Fig. 5**a** and Fig. 5**b** show the set of XRD diffraction pattern of the samples prepared at 750 °C and 850 °C, respectively, from 0.025 mol L^{-1} of precursor solution, while Fig. 5**c** and Fig. 5**d** shows equivalents XRD patterns for the materials obtained from 0.1 mol L^{-1} of precursor solution. Table 2 shows a summary of crystallite size and crystallinity of CT, CaKCT-0.2 and CaKCT-0.3 samples. The average crystallite sizes estimated by the Scherrer's equation for the CT samples prepared at 750 °C and 850 °C were close to 6 nm and 9 nm. On the other hand, CaKCT-0.2 and CaKCT-0.3 showed average crystallite sizes between 8 - 9 nm and 9 – 11 nm for the solid solutions obtained at 750 °C and 850 °C, respectively (Table 2**).** As a general fact, the higher the concentration of the precursor solution, the higher the average crystallite size, reaching a maximum of ca. 11 nm for CaKCT-0.3 at 850 °C using 0.1 mol L^{-1} of precursor solution. It can be seen from Table 2 that samples pyrolized at low temperature, 750 °C (Fig. 5**a** and Fig. 5c) showed a lower crystallinity degree than those pyrolyzed at 850 °C (Fig. 5**b** and Fig. 5d).

Table 2 shows that the crystallinity of the samples increases as function of the precursor solution concentration. The highest crystallinity (ca. 84%) was observed for the CaKCT-0.3 sample prepared at 850 °C from the highest concentrated solution (0.1 mol L^{-1}). The increase in the crystallinity agrees with the crystallite growth (Table 2) and can be associated with different factors such as the decrease of the surface defects, the redistribution of defects, and/or to the elimination of deformation at the microscale [82]. It is interesting to remark that the average crystalline size values (estimated from Scherrer´s equation) were close to 9 nm (Table 2) for the three materials, while SEM images (Fig. 1) showed much higher particles sizes. It means that the spherical materials are conformed by smaller crystalline units of the oxide, and therefore, the present titanate-based materials are nanostructured.

Table 3 shows a comparison between the particle size and average crystallite size of the present $CaTiO_3$-based materials and similar samples synthesized by different methods.

The particles size of the powders obtained by the present spray pyrolysis methodology are within the range reported for other method-

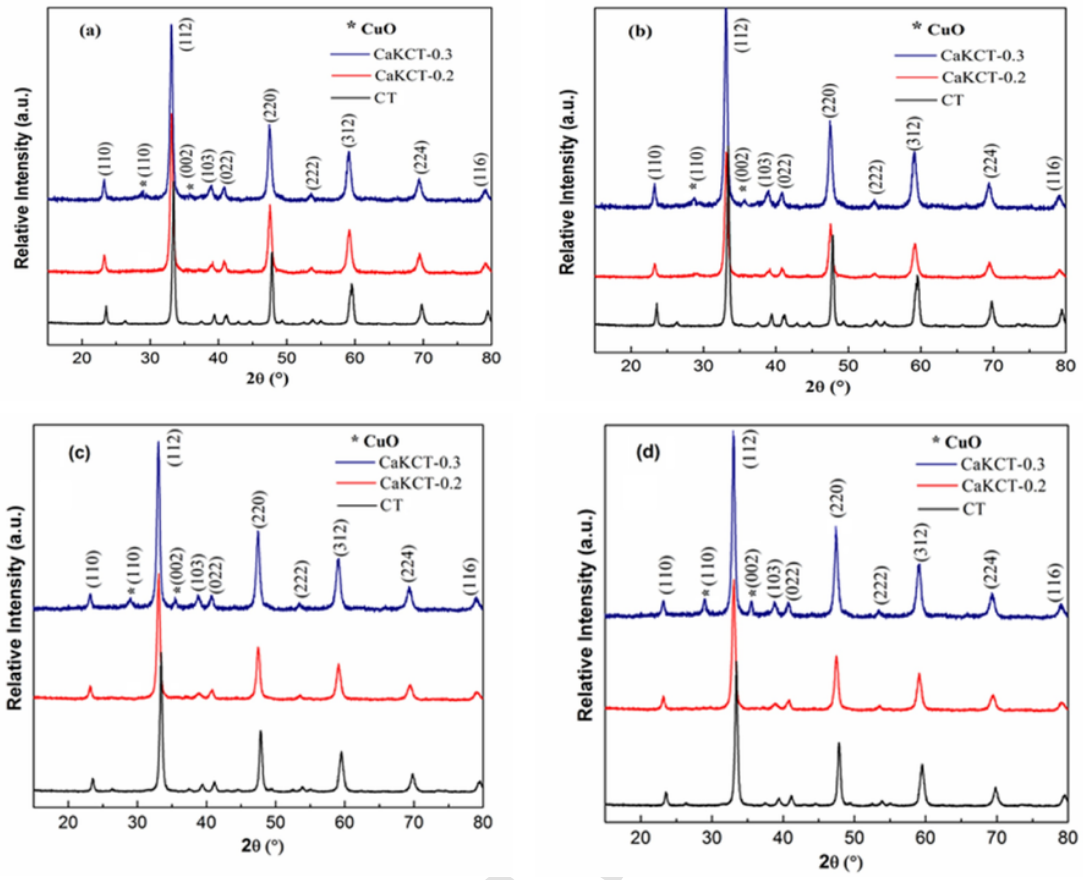

Fig. 5. XRD diffraction pattern of CT, CaKCT-0.2 and CaKCT-0.3 prepared at different temperatures and different precursor solutions. (a): 0.025 mol L^{-1} and 750 °C. (b) 0.025 mol L^{-1} and 850 °C. (c): 0.1 mol L^{-1} and 750 °C. (d) 0.1 mol L^{-1} and 850 °C.

Table 2
Summary of crystallite size and crystallinity of CT, CaKCT-0.2 and CaKCT-0.3 samples as a function of the concentration of the precursor solution and pyrolysis temperature.

Sample	Concentration (mol L^{-1})	Temperature (ºC)	Crystallite size (nm)	Crystallinity (%)
CT	0.025	750	5.7	59
CT	0.025	850	8.7	64
CT	0.1	750	8.7	74
CT	0.1	850	9.2	78
CaKCT-0.2	0.025	750	8.0	61
CaKCT-0.2	0.025	850	9.0	72
CaKCT-0.2	0.1	750	9.2	77
CaKCT-0.2	0.1	850	10.2	80
CaKCT-0.3	0.025	750	8.9	67
CaKCT-0.3	0.025	850	9.9	70
CaKCT-0.3	0.1	750	9.6	75
CaKCT-0.3	0.1	850	10.7	84

ologies [26,51,83,87,88,90,91,93–98]. On the contrary, the present materials developed smaller crystallite size than those observed in the reported works [53,83–86,89,92]. This is an additional advantage of the present methodology of synthesis.

The set of structural parameters of CT, CaKCT-0.2 and CaKCT-0.3 powders were determined by the Rietveld method [64]. The XRD patterns were indexed based on the orthorhombic unit cell. Refinements were carried out for the powders obtained at 850 °C from precursor solutions of concentration 0.1 mol L^{-1} since these powders showed the highest crystallinity index, a necessary condition for a good refinement. In the structural refinement, the occupation sites for CT were 4c for Ca/O1, 4b for Ti and 8d for the Ca/O2 [59]. Both CaKCT-0.2 and CaKCT-0.3 solid solutions were refined considering the occupation of 4c sites for Ca/K/Cu/O1. The crystallographic data including the space group, lattice parameter and unitary cell volume are listed in Table 4.

Due to the increase in the concentration of K^+ and Cu^{2+} cations in the CT host structure, the cell parameters become smaller, and the distance between Ti and O is then shorter, increasing the Ti-O bond strength [79,80]. This fact agrees with the shift observed in the FTIR spectra (Fig. 4) for the Ti-O stretching from 563 cm^{-1} in the CT to 582 cm^{-1} in CaKCT-0.2 and CaKCT-0.3.

Fig. 6 shows that after the substitutions of Ca with K and Cu, the XRD diffraction lines of solid solutions (Fig. 5) are shifted toward lower angles as compared to $CaTiO_3$ [99]. Furthermore, from the CaKTC-0.3 solid solution in the Fig. 5, a small amount of a second phase was identified as CuO of monoclinic symmetry. An increase in the relative intensity of this phase is observed in the Fig. 5**c** and Fig. 5**d**. This behavior suggests a low capability of the solid solution to incorporate all the Cu^{+2} cations into the crystalline lattice for the $x \geq 0.3$. In this sense, an exudation phenomenon of Cu particles to the surface following oxidation can occur during the cooling down to room temperature.

From the refined parameters [84] listed in the Table 4, the graphic representations of the unit cell of the samples were constructed. Fig. 7 shows the view along the (001) axis which represents the bond distances for CaKCT-0.2 (Fig. 7a), CaKCT-0.3 (Fig. 7b). Both structures

Table 3
Comparisons of the particle size and average crystallite size of $CaTiO_3$-based materials prepared by different methodologies.

Compound	Synthesis Method	Particles Size (μm)	Crystalline Size (nm)	Crystallinity (%)	Ref.
CT	Spray Pyrolysis	0.2 - 0.6	6 - 9	59 - 78	This work
CaKCT-0.2	Spray Pyrolysis	0.2 - 0.6	8 - 10	61 - 79	This work
CaKCT-0.3	Spray Pyrolysis	0.4 - 0.8	9 - 10	67 - 84	This work
$CaTiO_3$	Solid-State Reaction	17	---	---	[26]
$CaTiO_3$	Solid-State Reaction	0.3 - 2.3	---	---	[51]
$CaTiO_3$	Solid-State Reaction	0.1 – 0.2	70 - 120	---	[83]
$CaTiO_3$	Solid-State Reaction	---	32	---	[84]
$CaTiO_3$	High-Energy Ball Milling	---	90	---	[85]
$CaTiO_3$	Combustion Method	---	28	---	[86]
$CaTiO_3$	Plasma Sprayed	63 – 125	---	---	[87]
CaTiO	Polymeric Precursor Method	0.03 – 0.05	---	---	[88]
$CaTiO_3$	Polymeric Precursor Method	---	21 - 28	---	[89]
$CaTiO_3$	Sol-Gel Process	---	21 – 28	---	[53]
$CaTiO_3$	Sol-Gel Process	0.01 – 0.08	---	---	[90]
$CaTiO_3$	Sol-Gel Process	0.02 – 0.03	---	---	[91]
$CaTiO_3$	Microwave-Assisted Synthesis	---	37	---	[92]
$CaTiO_3$	Microwave-Hydrothermal	2	---	---	[93]
$CaTiO_3$	Hydrothermal Process	0.2 – 0.5	---	---	[94]
$CaTiO_3$	Hydrothermal Process	0.5 - 1.5	---	---	[95]
$CaTiO_3$	Hydrothermal Process	0.4	---	---	[96]
$CaTiO_3$	Solvothermal Process	0.6 – 1.4	---	---	[97]
$CaTiO_3$	Polyacrylamide Gel Route	0.02 – 0.07	---	---	[98]

Table 4
List of crystallographic data of CT, CaKCT-0.2 and CaKCT-0.3 samples obtained at 850 °C from 0.1 mol L^{-1} of precursor solution.

Crystallographic Data			
Sample	CT	CaKCT-0.2	CaKCT-0.3
Crystal System	Orthorhombic	Orthorhombic	Orthorhombic
Space group	Pbnm (62)	Pbnm (62)	Pbnm (62)
a [Å]	5.4332 (5)	5.4051 (10)	5.4371 (2)
b [Å]	5.4509 (9)	5.4344 (12)	5.4025 (3)
c [Å]	7.6570 (10)	7.6518(9)	7.6510 (3)
V [$Å^3$]	226.753 (8)	224.76 (7)	224.74 (3)
Rietveld Data			
U	0.2805	0.2908	0.2147
V	-0.1194	-0.1096	-0.0391
W	0.2839	0.0305	0.0208
X	3.96	-0.0025	-0.0007
R_{Bragg} (%)	4.89	7.64	8.63
R_F (%)	15.8	10.4	14.9
$_cR_p$ (%)	21.2	20.2	24.2
$_cR_{wp}$ (%)	5.43	20.8	22.8
χ^2	2.47	2.81	4.01

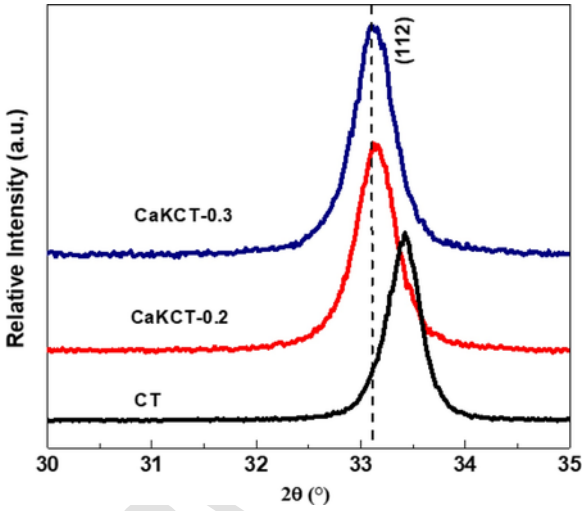

Fig. 6. . Shifting of XRD patterns of CaKCT-0.2 and CaKCT-0.3 to lower angles as compared to CT.

are similar than $CaTiO_3$ (Fig. 7c) reported previously [59]. In these structures, the octahedra are rotated on more than one cartesian axes, when compared to the ideal cubic perovskite [100]. However, the polyhedral [TiO_6] units in the CaKCT-0.2 and CaKCT-0.3 structures are tilted and distorted as function of doping of host structure with K^+ and Cu^{+2} cations which are in the 12-fold coordinated sites. The polyhedral views along (001) for the CaKCT-0.2 and CaKCT-0.3 powders are shown in Fig. 7**d** and Fig. 7e, respectively.

The structural refinement showed that Ti-O bond distances are not similar in the samples and the angle between O-Ti-O in the *ab* plane is also different than 180°. This is an evidence of the distortion of the octahedra, as shown in Fig. 7**a** and Fig. 7**b**. The rotation angle determined for the CaKCT-0.2 in the c-axis (Ti-O2-Ti) is equal to 155.44°, and the angle associated to (001) plane of the octahedral tilt is equal to 167.24°. For the CaKCT-0.3 the c-axis (Ti-O2-Ti) increase to 163.81° whereas the angle related to the octahedral tilt decrease to 145.20°. This can be associated with the Ti-O(2) bonds of 1.748 Å for the CaKCT-0.2 and 1.856 Å for the CaKCT-0.3, where is observed a compression of the polyhedron along of the equatorial plane (Fig. 7**a** and Fig. 7b). For the $CaTiO_3$ single crystal the angle of the c-axis (Ti-O2-Ti) and the angle relative to (001) plane are similar and equal to 155.72° and 156.68°, respectively, while the Ti-O(2) bonds equal to 1.955 Å, as shown in Fig. 7**c**. The length of the c-axis (Ti-O2-Ti) increases while the octahedral tilt angle is decreased when the substitutional x value increases. The differences in the angles in (Ti-O2-Ti) and in the octahedral tilt angles indicate a distortion of the octahedra. The distortion of octahedra due to the replacement of Ca cations by K and Cu cations could be intimately related with the catalytic activity of these materials, as discussed as follows.

3.2. Catalytic Production of FAEE´s

It has been reported [101] that the physical and chemical properties of CaO-based materials including the pore size distribution, the specific surface area, and chemical composition are directly related with the catalytic activity in the biodiesel production. The samples reported in the present work are constituted by hollow nanostructured sphere, and thus, it is important to remark this morphology can play an important role in the catalytic activity as dis as follows.

3.2.1. Preliminary tests

As a first approach, the catalytic tests for the synthesis of FAEE´s from soybean oil were carried out with a molar ratio of

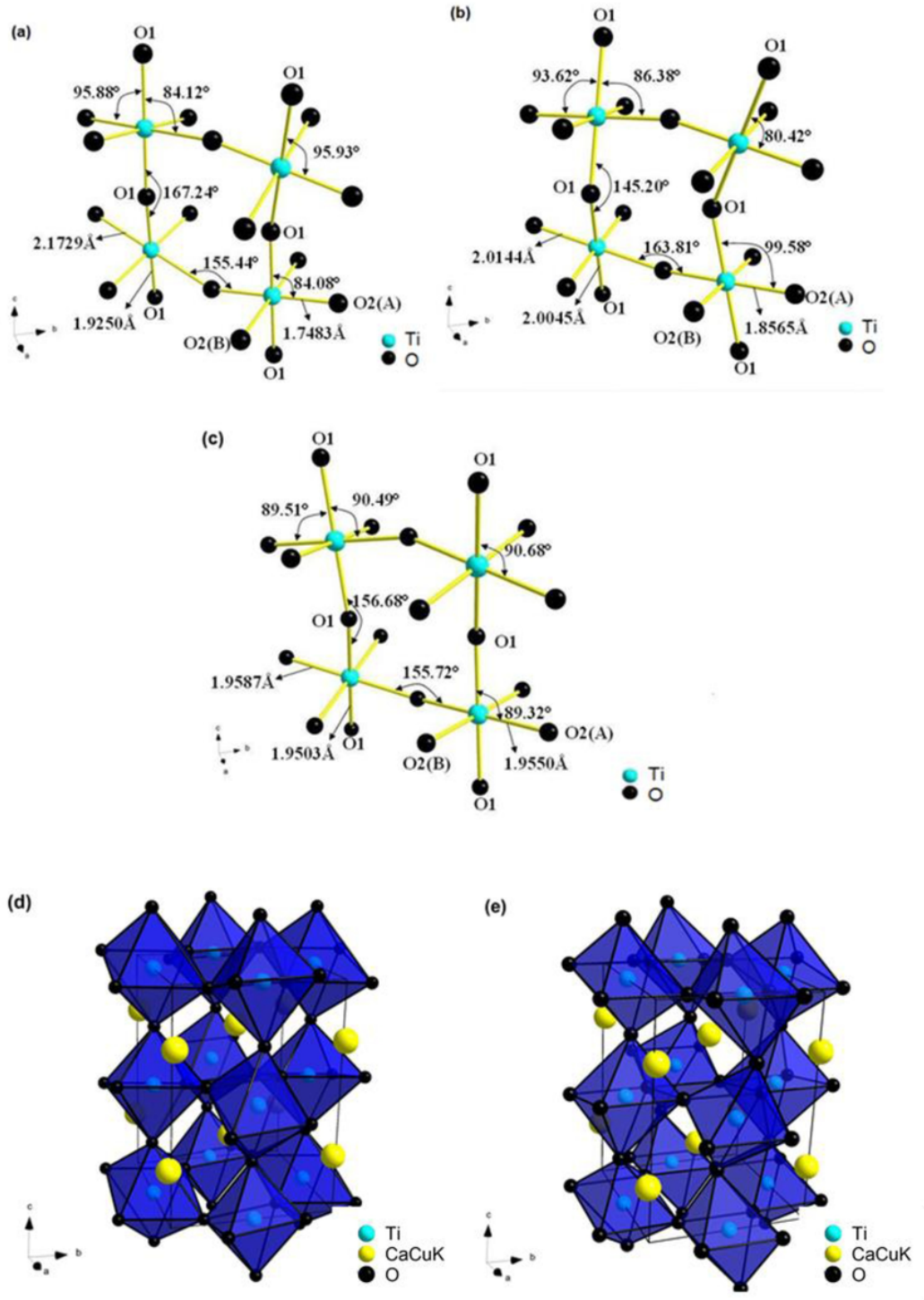

Fig. 7. View along the (001) axis which represents the bond distances. (a) CaKCT-0.2. (b) CaKCT-0.3 powders. (c) $CaTiO_3$ single crystal. Polyhedral view along (001) for the doped samples. (d) CaKCT-0.2. (e) CaKCT-0.3.

1:40 (oil:ethanol), at 120 °C, 40 bar of N_2 pressure and 15 wt.% of catalyst´s loading. Table 5 shows a summary of the catalytic activity observed after 24 h reaction for the CT, CaKCT-0.2 and CaKCT-0.3 samples prepared at 750 °C and 850 °C from 0.025 mol L^{-1} and 0.1 mol L^{-1} concentration of precursor solution.

According to the Table 5, all materials showed catalytic activity. The CT sample prepared at 750 °C from 0.025 mol L^{-1} concentration of precursor solution was the only sample with higher catalytic activity than its analogous prepared at 850 °C. All the K- and Cu-doped samples prepared at 850 °C from 0.1 mol L^{-1} concentration showed higher catalytic activities than the analogous samples prepared at 750 °C. In spite of the CT sample showed lower activities than CaKCT-0.2 and CaKCT-0.3 powders, it must be point out that CT showed a higher activity than the reported for $CaTiO_3$ samples prepared by solid-state reaction [26], where the yield to FAEE was negligible at 60 °C. The presence of CuO as an additional phase in the CT catalyst led to a higher perfor-

Table 5
Catalytic activity of CT, CaKCT-0.2 and CaKCT-0.3 samples for the synthesis of FAEE´s after 24 h reaction at 120 °C, 40 bar, and 15 wt.% loading.

Catalyst	Concentration (mol L^{-1})	Temperature (ºC)	Yield (%)
CT	0.025	750	30
CT	0.025	850	16
CT	0.1	750	16
CT	0.1	850	21
CaKCT-0.2	0.025	750	21
CaKCT-0.2	0.025	850	75
CaKCT-0.2	0.1	750	53
CaKCT-0.2	0.1	850	81
CaKCT-0.3	0.025	750	60
CaKCT-0.3	0.025	850	62
CaKCT-0.3	0.1	750	85
CaKCT-0.3	0.1	850	89

mance on the catalytic activity in the FAEE´s production. In this sense, CuO seems to play the role of a basic catalyst [26].

The analysis of the present catalysts by the Hammett´s method revealed the presence of basic sites in all the samples (color change of the suspension at high pKa). Data in the **Table S2** (**supplementary material**) indicate that the CaKCT-0.3 catalyst exhibited the less basic chemical nature since this sample showed the lowest titrations at $pK_a = 9.8$. This fact agrees with a higher substitution of Ca cations by K and Cu cations at the A-site of the $CaTiO_3$ host structure. Thus, the increase of concentration in Cu cation in the $CaTiO_3$ host structure seems to induce a less basic behavior of the catalyst. A similar trend is observed from the values of the FAEE´s yields in Table 5. The catalytic activity to produce FAEE´s increases with the doping of K and Cu cation in the $CaTiO_3$ host structure. As discussed above, one of the key factors can be the atomic radii and valence state of the A-cation. A correlation between the catalytic activity and the atomic number of the alkaline metal has been reported [102–103]. This phenomenon has been assigned to the increase of the electron density on the active sites due to the increase in the atomic radii of the doping atoms, which promotes a more efficient diffusion of electrons from the lattice oxygen of the catalysts. Thus, based on the substitution of Ca by K cation, the atomic radii r of the A-cation is increased, for instance, r(K) = 2.27 Å > r(Ca) = 1.97 Å. As discussed above from the XRD analysis, Cu particles diffused to surface, can be oxidized in the surface of the material leading to the formation of CuO. Therefore, CuO can act as an electron-donor catalytic component improving the catalyst performance. According to the structural analysis discussed above, the replacement of Ca cations by K and Cu cations at the A-site of the $CaTiO_3$ host structure, promotes an increase in the angle of the c-axis (Ti-O2-Ti) while the tilt of the octahedral angle decrease. The difference between both angles indicates a distortion of the titanium octahedron [TiO_6], which can be related with the polarization of the structure, promoting a higher chemical reactivity [24]. In this sense, the efficiency of the electron transfer depends on the distortion degree of Ti-O bonds. The higher the distortion in the structure, the higher is the polarization, and accordingly, the catalytic activity increase since the apical oxygen atoms in the structure (Fig. 6d and 6e) are more reactive as reported elsewhere [24].

Another important characteristic from the present samples refers to the formation of hollow spheres as discussed from SEM (Fig. 1) and TEM (Fig. 2) analysis. The formation of the hollows spheres is remarkable for CaKCT-0.2 and CaKCT-0.3 samples prepared at 850 °C with an initial concentration of 0.1 mol L^{-1} of precursor solution. By contrast, hollow spheres were not observed for the CT sample. Thus, the remarkable higher catalytic activity observed on CaKCT-0.2 and CaKCT-0.3 can be ascribed to the presence of these hollow spaces, that together with the texture can promote a higher degree of interaction between the triglycerides of the soybean oil and the catalytic active sites. The contribution of the mesopore volume to the total pore of volume in CaKCT-0.2 and CaKCT-0.3 samples increase together with the mean pore diameter (Table 1). This higher mean pore diameter together with the develop of a higher mesopore framework within the spheres (Fig. 3), would permit an effective diffusion of soybean oil molecules from the bulk of solution, increasing the interaction with the active sites. A similar influence of the morphology upon the catalytic activity has been reported for C-doped Pt-RuO_2 [104] hollow spheres, and more recently, by a spinel-based on $CoCr_2O_4$ spherical samples [105]. Considering the best catalytic activity was reached for the CaKCT-0.3 catalyst prepared at 850 °C from 0.1 mol L^{-1} of precursor solution, a careful study for the catalytic production of FAEE´s was performed as a function of the reaction time, the weight of catalysts, temperature, pressure, and the reuse of samples.

3.2.2. *Influence of reaction time and catalysts loading*

Fig. 8**a** shows the FAEE´s production at 120 °C and 40 bar pressure as a function of reaction time. CaKCT-0.2 and CaKCT-0.3 catalysts are clearly more active than CT. The maximum FAEE´s yield after 24 h reaction achieved 89 % and 81 % on CaKCT-0.3 and CaKCT-0.2 catalysts, respectively. By contrast, only 21 % of FAEE´s yield was observed after 24 h over the CT catalyst.

As discussed above, the polarization of the present perovskite-like structures can promote a higher reactivity [24] leading to an increase in the catalytic activity [73,104]. In addition, it has been reported that the catalytic activity on Ti-based catalysts is favored by the presence of mesopores in the pore framework [73]. Accordingly, the higher cat-

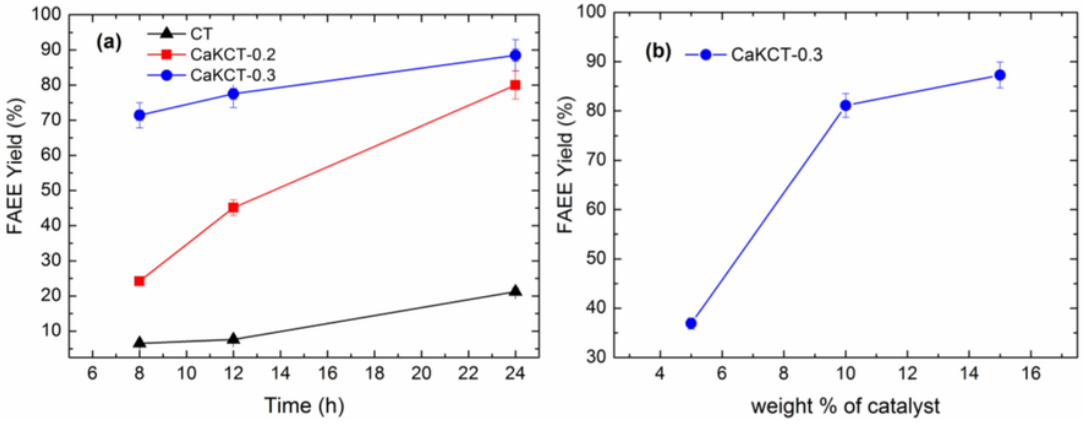

Fig. 8. FAEE yields at 120 °C and 40 bar pressure. (a): Kinetics of FAEE´s production on CT, CaKCT-0.2 and CaKCT-0.3 catalysts. (b): Influence of the catalysts loading using the CaKCT-0.3 catalyst.

alytic activity presented by the CaKCT-0.2 and CaKCT-0.3 samples seems to be associated with the presence of mesoporous hollow particles. A large mean pore size and an important contribution of mesopores to the total pore of volume promote an efficient diffusion of the triglyceride's molecules of soybean oil from the bulk solution to the active catalytic sites. It can be seen from Fig. 8**a** that the kinetics of FAEE´s formation on the CT sample requires a long induction period to yield a representative production of FAEE. On the contrary, CaKCT-0.2 and CaKCT-0.3 are activated in shorter reaction times. This observation is reinforced by the comparison between the values of the initial reaction-rates (v_0) and the first-order apparent rate-constants (k_{app}). A summary of the kinetic parameters obtained for the FAEE´s production is listed in the Table 6.

Keeping in mind the initial concentration of soybean oil is ca. 0.43 mol L^{-1}, using the data from Fig. 8a, the initial reaction-rates (v_0) are 0.006 mol L^{-1} min^{-1}, 0.022 mol L^{-1} min^{-1}, and 0.064 mol L^{-1} min^{-1}, for CT, CaKCT-0.2 and CaKCT-0.3, respectively. These values represent an enhancement in the initial catalytic activity (A_{vo}) relative to CT equal to 3.7 and 10.7 for CaKCT-0.2 and CaKCT-0.3, respectively. This is strong kinetic evidence that the hollow spheres and the broad pore size distribution in the present samples can be responsible of the enhancement in the diffusion of soybean oil molecules from the bulk solution, and accordingly, the induction kinetic period for the activation of the catalysts is clearly lower. The comparison between the pore diameter (Table 1) and v_0 (Table 6) clearly shows that the initial reaction-rate is a direct function of the pore diameter of the catalysts demonstrating this particular morphology in the shape of hollow spheres is responsible of the enhancement in the catalytic activity. This phenomenon was early reported by Abdullah and coworkers [106] for the transesterification of palm oil using mesoporous K/SBA-15 catalysts.

On the other hand, considering 12 h of reaction, the first-order apparent rate-constants (k_{app}) were estimated. These values are equal to ca. 0.006 min^{-1}, 0.027 min^{-1}, and 0.049 min^{-1}, for CT, CaKCT-0.2 and CaKCT-0.3, respectively. It is interesting to point out that for the CT catalyst k_{app} is similar to v_0, indicating that mass diffusion is the determining-step of the reaction on this catalyst. On the contrary, k_{app} was slightly higher than v_0 on CaKCT-0.2 sample but clearly lower on CaKCT-0.3 sample. This is strong evidence that after complete the induction kinetic period (about 8 h), CaKCT-0.2 became a more active catalysts while CaKCT-0.3 decrease the catalytic activity due to a saturation of the active sites since this catalyst does not present limitations in the diffusion of molecules from the bulk of solution. Accordingly, in terms of k_{app}, the enhancement in the catalytic activity relative to CT (A_{kapp}) is ca. 4.5 and 8.2 for CaKCT-0.2 and CaKCT-0.3, respectively. It can be concluded that the CaKCT-0.3 sample prepared at 850 °C from 0.1 mol L^{-1} of the precursor solution is the best catalysts since it achieved practically the same catalytic activity (78 %) than CaKCT-0.2 (81 %) in only 12 h while the CaKCT-0.2 catalyst required 24 h. Accordingly, this sample was selected for the following catalytic studies.

Fig. 8**b** shows the yields to FAEE´s production as a function of the catalysts loading, 5, 10 and 15 wt.%. The FAEE´s yield was evaluated at 120 °C and, 40 bar and after 24 h reaction. According to Fig. 8b, the catalytic activity was ca. 37 %, 81 % and 89 % using 5, 10 and 15 wt.%, respectively. It indicates that the interaction of the triglyceride molecules with the active sites of the catalyst is clearly favored with the increase in the loading of catalyst. It has been reported this enhancement in the catalytic activity is consequence of an increase in the rate of diffusion of molecules from the bulk of solution [106] due to a higher concentration of catalytic active sites. A similar behavior was reported by Al-Shammari and coworkers [107] showing that the increase in the catalytic activity of La-exchanged Keggin structured heteropoly compounds for biodiesel production is influenced by the increase in the number of basic sites. The results obtained of the acid/base titration (**Table S2**, **appendix**) and textural properties (Table 1) of the present samples agree with the results reported by these authors.

Table 6
Summary of kinetic parameters obtained for the FAEE´s production.

Samples	v_0 [a] (mol L^{-1} min^{-1})	A_{vo} [b]	k_{app} [c] (min^{-1})	R^2 [d]	A_{kr} [e]
CT	0.006	1.0	0.006	0.993	1.0
CaKCT-0.2	0.022	3.7	0.027	0.981	4.5
CaKCT-0.3	0.064	10.7	0.049	0.938	8.2

[a] Initial reaction-rates (v_0). [b] A_{vo} is the initial catalytic activity relative to CT in terms of v_0. [c] First-order apparent rate-constants (k_{app}). [d] Quadratic factor from the linear regression. [e] A_{kapp} is the catalytic activity relative to CT in terms of k_{app}.

However, it must be point out that the FAEE´s yields obtained after 24 h reaction using 10 wt.% and 15 wt.% of catalysts loading are practically similar, thus, the costs of the FAEE´s production could be lower using 10 wt.% catalysts. Thus, a further economic analysis should be performed to verify this point, but it is not part of the objectives of the present work.

The FAEE´s synthesized after 24 h of reaction using CaKCT-0.3 catalyst was analyzed by GC-FID (**Table S3, Supplementary information**) and MS-GC. It can be seen from **Figure S5 (supplementary**) that the FAEE´s is mainly composed by five different components. The analysis performed by MS-GC (**Figure S6, supplementary**) confirmed the formation of the following fatty acid ethyl esters: palmitic, stearic, oleic, linoleic, and linolenic, respectively. The order and percentual proportion of products detected was the following: linoleic (44 %) > oleic (26 %) > palmitic (17 %) > linolenic (7 %) > stearic (6%). Thus, 83% of the total FAEE´s corresponds to linoleate + oleate + palmitate blend suggesting a good homogeneity of the FAEE´s and accordingly, a great potential as biodiesel fuel. Similar composition has been reported by Da Silva and coworkers [108] for the synthesis of FAEE´s from soybean oil by the methylic route.

3.2.3. Influence of temperature and pressure

Fig. 9 shows the influence of temperature and pressure upon the catalytic activity of the CaKCT-0.3 catalyst, evaluated after 24 h reaction and using 15 wt.% catalyst loading. Fig. 9**a** shows the variation of temperature using 60 °C, 80 °C, 100 °C and 120 °C, at 40 bar pressure of N_2. At 60 °C, the FAEE´s yield was only ca. 7 %. However, this yield is even higher than that reported [26] using $CaTiO_3$-based catalysts at the same temperature. Fig. 9**a** shows that FAEE´s yield is strongly influenced by the temperature showing a remarkable increase up to ca. 42 %, 79 % and 89 % at 80 °C, 100 °C, and 120 °C, respectively. These results suggest that at least 100 °C must be used to activate the CaKCT-0.3 catalyst.

Considering the initial reaction rate (v_0) in terms of the FAEE´s yields, the activation energy was estimated using the Arrhenius´ formulism [49,109]. The value obtained for the activation energy using the CaKCT-0.3 catalyst at 40 bar pressure was ca. 11.0 kcal mol^{-1} which is not so different than 9.0 kcal mol^{-1} reported for the synthesis of FAEE´s from waste frying oil using a $CuFe_2O_4$-based nanocatalyst [49]. However, the present value is 1.7 times higher than 6.6 kcal mol^{-1} reported for a mixture of FAEE´s produced from the almonds of *Syagrus cearensis* using KOH as catalyst [109]. This result is expected since KOH is a more active catalysts due to the high basic pH but at the same time it is a corrosive catalyst.

In addition, the FAEE´s production was also monitored at 120 °C using three different pressures 1, 20, and 40 bar. The results are shown in the Fig. 9**b**. Under atmospheric pressure the FAEE´s yield was only ca. 60 %, while at 20 bar, the FAEE yield was ca. 80%, very close to the maximum value obtained using 40 bar, ca. 89 %. It has been reported that the influence of the pressure in the transesterification of oils is negligible under the supercritical condition, which is commonly higher than 200 bar [110]. However, it can be seen from Fig. 9**b** that the

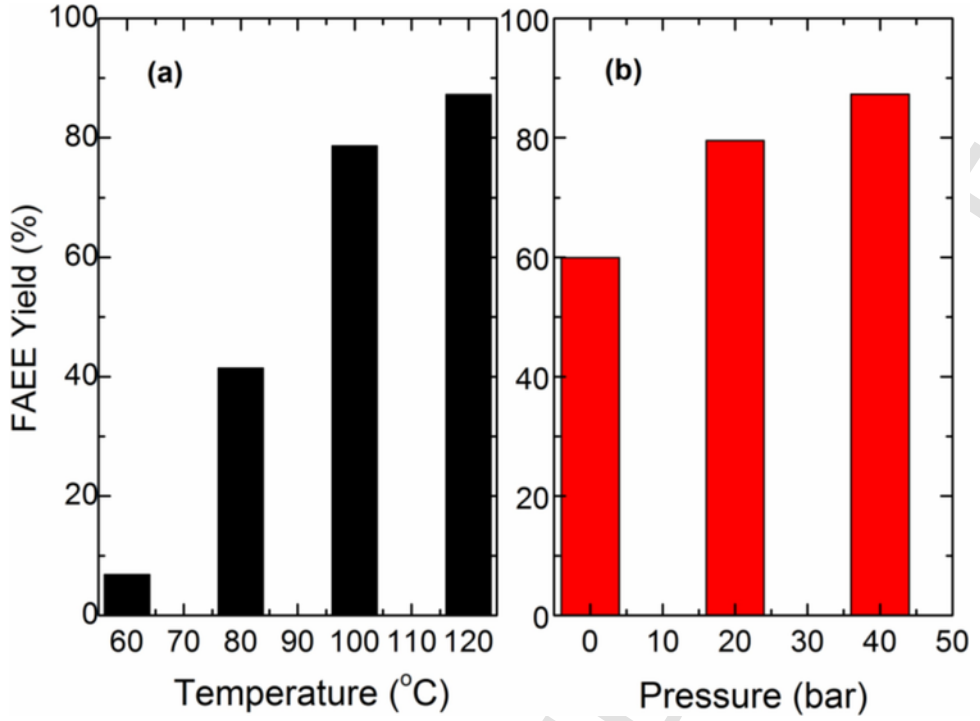

Fig. 9. FAEE´s yields after 24 h reaction using 15 wt.% loading of CaKCT-0.3 catalyst. (a): Effect of the temperature at P = 40 bar. (b): Influence of pressure at T = 120 °C.

yield of FAEE´s did change with the pressure since the pressure range of the present study is far from the supercritical condition. Though a more detailed economic balance for the costs of the FAEE´s prepared should be performed, it can be concluded that the best conditions for the CAKCT-0.3 catalysts are 15 % loading, 120 °C and 40 bar pressure.

Although both temperature and pressure influence the synthesis of FAEE´s from soybean oil transesterification reaction, the effect of temperature seems to be more important upon the activity of the catalysts. The influence of the temperature can be associated to the internal energy of one or more components in the raw material, oil and alcohol. In this sense, a critical temperature must be achieved to activate the catalysts, but also, the increase of temperature can influence the viscosity of a liquid, which is directly proportional to the attraction force between the molecules. In this sense, the higher the temperature of reaction the lower the viscosity. Accordingly, an increase in the mass transfer from the bulk of solution to the pores of catalysts can be responsible of an enhancement in the interaction between the triglyceride molecules and the active sites of the catalyst, and thus, increasing the catalytic activity.

Concerning to the order of reaction, it has been recently reported [111] that the second order model gives an appropriate description of the biodiesel production using KOH and CaO catalysts. In the present study the order of reaction cannot be directly verified since the proportion between ethanol and soybean oil remains constant with a ratio 40:1, and thus the soybean concentration was constant. However, some approximation can be made keeping in mind the reactions involved in the production of FAEE´s takes place in different steps, one of them including the initial interaction of the alcohol with the catalysts to produce the alkoxide which in a second step interacts with the oil to produce the mixture of FAEE´s. The apparent order of reaction for the FAEES´s production can be estimated from the initial rates (v_o) as a function of the catalysts loading (L_{cat}). For the case of the best catalysts (CaKCT-0.3), the linear regression given by the expression: [$\log(v_0) = \log(k_r) + n.\log(L_{cat})$], yields a slope of ca. 0.883 with a regression factor of 0.941. This slope is close to the unit indicating that the order of reaction seems to follow a first-order mechanism, at least in terms of the catalysts loading.

3.2.4. *Stability of catalysts: Reuse and leaching studies*

The stability of the CaKCT-0.3 catalysts was verified by performing three consecutive catalytic runs of transesterification reaction of soybean oil with ethanol over 24 h at 40 bars of N_2 and 120 °C for 15 wt.% loading of catalyst. After the first catalytic run (R1), the catalyst was separated from the mixture by successive processes of centrifugation following washing with hexane. This procedure permits to obtain a catalyst without residues of the transesterification´s products. This was verified by GC-FID analysis of the filtrated solvent (hexane) after washing the catalyst (**Figure S7, Appendix**). This procedure was performed in each reuse of the catalyst. The catalyst was subsequently heated in an oven at 100 °C for one hour before the following catalytic run. As discussed above, in the first catalytic run the FAEE´s yield was ca. 89 % decreasing to 81 % and 77 %, respectively, after the second and third catalytic runs. The loss of activity can be explained by a possible poisoning by the irreversible adsorption of some fraction of the fatty acid on the active sites of the catalyst. Nevertheless, the present study permits to extrapolate a long-term stability up to 15 consecutive catalytic reuses of the CaKCT-0.3 catalyst.

Finally, the leaching of K and Ca from catalysts was verified. The analysis of K and Ca was performed by flame atomic absorption spectrometry (FAAS) and the results are compiled in the Table 7.

The FAEE´s produced at the first run (R1) using CT and CaKCT-0.2 catalysts showed that Ca and K concentrations are lower than the limit of detection. By contrast, Ca and K were detected in all the catalytic runs using the CaKCT-0.3 catalysts, but these concentrations are adjusted to the values required by the Brazilian legislation for the synthesis of biodiesel production. In terms of the initial content of K and Ca in the $Ca_{0.7}K_{0.3}TiCu_{0.15}O_3$ catalyst, the accumulated leaching observed for K and Ca after 3 consecutive catalytic runs was only 1.2 and 0.09 wt. %. Thus, it can be concluded the present catalysts showed a strong resistance to be leached during the synthesis of FAEE´s.

Table 7
Ca and K detected in the FAEE´s after consecutive catalytic runs.

Samples	Potassium (mg kg^{-1}) [a]		Calcium (mg kg^{-1}) [a]	
	Average [a]	± σ [b]	Average [a]	± σ [b]
CT (R1) [d]	< LOD [c] ---		< LOD [c] ---	
CaKCT-0.2 (R1) [d]	< LOD [c] ---		< LOD [c] ---	
CaKCT-0.3 (R1) [d]	3.7	± 0.5	0.90	± 0.02
CaKCT-0.3 (R2) [e]	2.7	± 0.1	0.85	± 0.02
CaKCT-0.3 (R3) [f]	2.1	± 0.1	0.84	± 0.01

[a] Average values for triplicate analysis. [b] σ is the standard deviation. [c] < LOQ means values of K and Ca were lower than the limit of detection. [d] R1: values obtained in the first catalytic run. [e] R2: values for the second catalytic run. [f] R3: values for the third catalytic run.

3.2.5. General discussion

The composition of the FAEE´s was determined from the MS-GC studies discussed above, but some aspects about the fuel properties and quality of the FAEE´s should be verified to visualize its potential as biodiesel to be used in diesel engines [112]. A complete analysis of the fuel properties of the FAEE´s mixture requires ca. 350 mL which is far from our actual possibilities (ca. 30 mL by catalytic test). Keeping this in mind, the future research will perform a scale-up study with the best catalyst and the optimal conditions and the biodiesel fuels properties including the Acid Number (ASTM D664), Ash, Sulfated Residue (ASTM D874), Carbon Residue (ASTM D524), Cetane Number (ASTM D613), Cloud Point (ASTM D2500), Copper Corrosion (ASTM D130), Distillation at Reduced Press (ASTM D1160), Flash Point (ASTM D93), Free & Total Glycerin (ASTM D6584), Oxidation Stability (ASTM D2274), Pour Point (ASTM D97 / D5950), Sediment & Water (ASTM D1796/D2709), Sulfur Content (ASTM D4294), Spectrochemical (ASTM D6728) and Viscosity (ASTM D445), will be determined to verify if the present FAEE´s meets with the ASTM and OEM blending and product handling specifications for a biodiesel fuel. However, to clarify this important point, some properties of the FAEE´s produced such as specific mass and kinematic viscosity were primary analyzed to visualize the potential of this mixture as biodiesel. Table 8 shows the results obtained for the FAEE´s mixtures produced after 24 h reaction using 15 wt. % catalysts, 120 °C and 40 bars. For comparative reasons, the two best catalysts were included in this analysis. The deviations relative to the average specific mass standard (875 kg m^{-3}) are only ca. 0.8 % and 0.9 % for the FAEE´s produced using CaKCT-0.2 and CaKCT-0.3, respectively. On the contrary, the deviations relative to the average kinematic viscosity (4.5 mm s^{-1}), are ca. 32 % and 2 % for the FAEE´s produced using CaKCT-0.2 and CaKCT-0.3, respectively. Thus, though both FAEE´s produced using CaKCT-0.2 and CaKCT-0.3 catalysts are within the range expected for a biodiesel according to the Brazilian standards. It is interesting to remark the correlation observed between the catalytic activity and the FAEE´s composition with the kinematic viscosity and specific mass. For instance, the FAEE´s blend obtained at the highest catalytic activity observed on the CaKCT-0.3 catalyst presented the lowest specific mass and the lowest kinematic viscosity, with only ca. 1% and ca. 3% of relative deviation with respect to the average values of the standards. Accordingly, it can be concluded that the mixture of FAEE´s obtained using the CaKCT-0.3 catalyst showed the best quality to be used as a potential biodiesel.

These properties are two of the most important parameters that affect the engine performance and the emission characteristics [113]. One of the major problems of the biodiesel-based engine is caused by the high viscosity of the fuel. Higher viscosity can cause poor fuel atomization during spray, increasing the carbon deposition on fuel filter and demanding more energy from the fuel pump [114]. A high kinematic viscosity is responsible for the slow diffusion through the filter and the fuel lines, which means that the FAEE mixture does not burn completely in the engine. In addition, a high viscosity of biodiesel fuel affects the start of injection, injection pressure and the fuel spray characteristics, which are the main parameters related with the engine performance and exhaust emission [115]. The specific mass or density of the diesel fuel is also an important parameter, since it is related with the cetane number and heating value that affect the performance of the engine [116].

Table 8
Specific mass and kinematic viscosity of the FAEE´s produced after 24 h reaction using 15 % catalysts, 120 °C and 40 bars.

Catalyst	Specific mass at 20 °C (kg m^{-3})	Method	Specification [c] (kg m^{-3})
CaKCT-0.2; CaKCT-0.3	882; 867	NBR 14065:2013 [a]	850 - 900
Catalyst	**kinematic viscosity at 40 °C (mm^2 s^{-1})**	**Method**	**Specification [c] (mm^2 s^{-1})**
CaKCT-0.2; CaKCT-0.3	5.94; 4.39	ASTM D 445.2017 [b]	3.0 - 6.0

[a]NBR 14065:2013. This is the set of standards from the Brazilian Association of Technical Standards (ABNT) for determining the specific mass, density and petroleum distillates and viscous oils that can normally be handled as liquids at test temperatures, using manual or automatic sample injection equipment. Its application is limited to liquids with vapor pressure below 100 kPa and viscosity below 15000 mm^2 s^{-1}). [b]ASTM D 445.2017 is the standard Test Method for Kinematic Viscosity of Transparent and Opaque Liquids (and Calculation of Dynamic Viscosity). This test method specifies a procedure for the determination of the kinematic viscosity of liquid petroleum products, both transparent and opaque, by measuring the time for a volume of liquid to flow under gravity through a calibrated glass capillary viscometer. The dynamic viscosity can be obtained by multiplying the kinematic viscosity by the density of the liquid. [c] The specifications are given according to the Resolution number 45 of the National Petroleum Agency (ANP no. 45, 25/08/2014), which provides for the specification of biodiesel contained in ANP Technical Regulation No. 3 of 2014 and the obligations regarding quality control to be attended by the various economic agents that sell the product throughout the national territory.
a

It should also be mention that due to the surface area of the best catalysts (CaKCT-0.3) is low (ca. 44 m^2 g^{-1}), the catalytic activity seems to be intimately related to the replacement of Ca cations by K and Cu cations at the A-site of the $CaTiO_3$ host structure. As discussed above, the increase of Cu cation concentration in the $CaTiO_3$ host structure induced a change in the behavior of the catalyst. Furthermore, the migration of CuO to the surface of the material, as reported in XRD diffraction analysis, can operate as co-catalyst improving the catalyst performance. In according to structural analysis, the replacement of Ca cations by K and Cu cations at the A-site of the $CaTiO_3$ host structure, the angle of the c-axis Ti-O2-Ti increase and the octahedral tilt angle decrease. The difference between both angles indicates a distortion of [TiO6] octahedra, promoting the polarization of the structure influencing the chemical reactivity. Thus, an increase in the catalytic activity is expected with the increase of in the polarization of the structure. In this sense, the higher the content of such distorted Ti-O bond, the higher is the efficiency of the electron transfer with a concomitant increase in the catalytic activity. The CaKCT-0.3 catalyst synthesized by the spray pyrolysis method and reported by the first time in the present work, showed advantages when compared with $CaTiO_3$ reported [26] prepared by the solid-state reaction, where the yield was close to zero at low temperature (60 °C). In comparison to other catalysts used to produce biodiesel under moderate reaction conditions [46–50], the present CaKCT-0.3 catalyst showed an excellent yield up to 89 % to produce fatty acid ethyl esters (FAEE´s) as potential biodiesel. It should be mention that the potential use of the present FAEE´s mixture in diesel engines must present biodegradable characteristics to be considered as an ecological fuel. These analyses will be also considered in a future work.

4. Conclusions

Titanate powders, $CaTiO_3$, $Ca_{0.8}K_{0.2}Cu_{0.10}TiO_3$ and $Ca_{0.7}K_{0.3}Cu_{0.15}TiO_3$, with hollow particles were synthesized by spray pyrolysis method and studied in the catalytic synthesis of FAEE´s as potential biodiesel. XRD patterns and SEM/TEM images permits to conclude the spherical materials are conformed by smaller crystalline units of the oxide, and thus, they are nanostructured. The increase of K and Cu concentration in the host structure of the $CaTiO_3$ and the formation of hollow spheres with a mesopore framework suggest an efficient behavior for the transesterification reaction of the soybean oil. Accordingly, carefully studies of the influence of time of reaction, catalysts loading, temperature, pressure and reuse of catalysts were performed. The high catalytic activity observed in the CaKCT-0.2 and CaKCT-0.3 samples with respect to the non-doped titanate has been associated with the presence of an important contribution of mesoporous hollow spheres and to a higher polarization of the structures yielding a more active catalysts due to the exposition of the active sites. The initial reaction-rate is a direct function of the mean pore diameter of the catalysts demonstrating that the morphology in the shape of hollow spheres of the present samples is responsible for the enhancement in the catalytic activity. CaKCT-0.3 was the best catalysts at 15 wt.% loading, 120 °C and 40 bar pressure. Though a more detailed economic balance and a fuel properties characterization for the FAEE´s produced must be performed, it can be concluded that K-and Cu-doped $CaTiO_3$-based nanostructured catalysts have a great potential to be used in the sustainable production of biodiesel.

Declaration of Competing Interest

We declare that the present work is approved for publication by all co-authors and the responsible authorities, where the work was carried out.

Acknowledgements

Authors thank to the grants # 07/03510-9; 14/11189-0; 19/06623-6; 02/05997-9 São Paulo Research Foundation (FAPESP) and CNPq for the financial support; Multiuser Laboratory of High Resolution Microscopy (LabMic) by the TEM measurements, L.P.M. Simões for X- ray diffraction measurements assistance and M.A.M.S. Da Veiga for chemical analysis by Flame Atomic Absorption Spectrometry (FAAS). P.S. Poon thanks: ANID-PIA/APOYO CCTE AFB170007. J. Matos acknowledges the Chilean project: ANID-FONDECYT 1190591 and the Millennium Science Initiative of the Ministry of Economy, Development and Tourism, Chile, grant Nuclei on Catalytic Processes towards Sustainable Chemistry (CSC).

Appendix A. Supplementary data

Supplementary material related to this article can be found, in the online version, at doi:https://doi.org/10.1016/j.apcatb.2020.118986.

References

[1] R.H. Mitchell, Perovskites: Modern and Ancient, Almaz Press, Ont., Canada, 2002.
[2] C.A. Triana, L.T. Corredor, D.A. Landínez Téllez, J. Roa-Rojas, High temperature-induced phase transitions in Sr_2GdRuO_6 complex perovskite, Mater. Res. Bull 46 (2011) 2478–2483.
[3] R. Shaheen, J. Bashir, H. Rundlöf, A.R. Rennie, The crystal structure of CaLaMn-FeO_6 double perovskite, Mater. Lett. 59 (2005) 2296–2299.
[4] Y.P. Liu, S.H. Chen, H.R. Fuh, Y.K. Wang, First-principle calculations of half-metallic double perovskite $La_2BB´O_6$(B,B´ = 3dtransition metal), Commun. Comput. Phys 14 (2013) 174–185.
[5] M.T. Anderson, K.B. Greenwood, G.A. Taylor, K.R. Poeppelmeier, B-cation arrangements in double perovskites, Prog. Solid State Chem 22 (1993) 197–233.
[6] L. Zhang, Q. Zhou, Q. He, T. He, Double-perovskites $A_2FeMoO_{6-\delta}$ (A = Ca, Sr, Ba) as anodes for solid oxide fuel cells, J. Power Sources 195 (2010) 6356–6366.
[7] S. Vasala, M. Lehtimaki, Y.H. Huang, H. Yamauchi, J.B. Goodenough, M. Karppinen, Degree of order and redox balance in B-site ordered double-perovskite oxides, $Sr_2MMoO_{6-\delta}$ (M = Mg, Mn, Fe, Co, Ni, Zn),, J. Solid State Chem 183 (2010) 1007–1012.
[8] Z. Zeng, M. Greenblatt, J.E. Sunstrom, M. Crof, S. Khalid, Giant magnetoresistance in $CaCu_3Mn_4O_{12}$-based oxides with perovskite-type structure,, J. Solid State Chem 147 (1999) 185–198.
[9] X. Guo, S. Dai, Y. Zhou, G. Yang, Z. Chen, Colossal magnetoresistance effect in perovskite-type La–Sn–Mn–O epitaxial films, Appl. Phys. Lett 75 (1999) 3378–3380.
[10] Z. Zeng, M. Greenblatt, M.A. Subramanian, M. Croft, Large low-field magnetoresistance in perovskite-type $CaCu_3Mn_4O_{12}$ without double exchange, Phys. Rev. Lett. 82 (1999) 3164–3167.
[11] N.C. Bristowe, J. Varignon, D. Fontaine, E. Bousquet, Ph. Ghosez, Ferromagnetism induced by entangled charge and orbital orderings in ferroelectric titanate perovskites, Nat. Comm. 6 (2015) 6677–6682.
[12] M.R. Manju, V.P. Kumar, V. Dayal, Investigation of ferromagnetic properties in Fe/Co substituted $BaSnO_3$ perovskite stannates, Physica B: Condens, Mater. 500 (2016) 14–19.
[13] R. Siddheswarana, P. Šuttaa, P. Nováka, M. Netrvalová, A. Hendrych, O. Životský, In-situ X-ray diffraction studies and magneto-optic Kerr effect on RF sputtered thin films of $BaTiO_3$ and Co, Nb co-doped $BaTiO_3$, Ceram. Inter 42 (2016) 3882–3887.
[14] K.W. Lee, W.E. Pickett, Compensated half-metallicity in the trigonally distorted perovskite $NiCrO_3$, Phys. Rev. B 83 (2011), 180406.
[15] C.M. Fernadez-Posada, H. Amorin, C. Correas, O. Pena, M. Alguero, A. Castro, Mechanosynthesis and multiferroic properties of the BiFeO3–BiMnO3–PbTiO3 ternary system along its morphotropic phase boundary, J. Mater. Chem. C. 3 (2015) 2255–2265.
[16] K. Parida, S.K. Dehury, R.N.P. Choudhary, Structural, electrical and magneto-electric characteristics of complex multiferroic perovskite Bi0.5Pb0.5Fe0.5Ce0.5O3, J. Mater. Sci: Mater. Electron. 27 (2016) 11211–11219.
[17] S. Lanfredi, M.A.L. Nobre, Dielectric loss and phase transition of sodium potassium niobate ceramic investigated by impedance spectroscopy, Catal. Today 78 (2003) 529–538.
[18] J. Li, P.M. Haney, Optical spintronics in organic-inorganic perovskite photovoltaics, Phys. Rev. B 93 (2016), 155432.
[19] S. Majumdar, S. Van Dijken, Pulsed laser deposition of $La_{1-x}Sr_xMnO_3$: thin-film properties and spintronic applications, J. Phys. D: Appl. Phys 47 (2014), 034010.
[20] R. Hu, R. Ding, J. Chen, J. Hu, Y. Zhang, Preparation and catalytic activities of the novel double perovskite-type oxide La_2CuNiO_6 for methane combustion, Catal. Commun. 21 (2012) 38–41.
[21] F.E.L. Suárez, A. Bueno-López, M.J. Illán-Gómez, B. Ura, J. Trawczynski, Study of the uncatalyzed and catalyzed combustion of diesel and biodiesel soot, Catal. Today 176 (2011) 182–186.
[22] J. Matos, P.S. Poon, S. Lanfredi, M.A.L. Nobre, Functional nanostructured catalysts based on the niobates to the dry methane reforming and ethylene homologation reactions, Fuel 107 (2013) 503–510.
[23] S. Lanfredi, M.A.L Nobre, P.G.P Moraes, J. Matos, Photodegradation of phenol red on a Ni-doped niobate/carbon composite, Ceram. Inter. 40 (2014) 9525–9534.
[24] J. Matos, S. Lanfredi, R. Montaña, M.A.L. Nobre, M.C. Fernández de Córdoba, C.O. Ania, Photochemical reactivity of apical oxygen in $KSr_2Nb_5O_{15}$ materials for environmental remediation under UV irradiation, J. Coll. Inter. Sci. 496 (2017) 211–221.
[25] M.L. Tummino, E. Laurenti, F. Deganello, A.B. Prevot, G. Magnacca, Revisiting the catalytic activity of a doped $SrFeO_3$ for water pollutants removal: Effect of light and temperature, Appl. Catal. B: Environ. 207 (2017) 174–181.
[26] Z. Kesiĉ, I. Lukiĉ, M. Zdujiĉ, C. Jovalekic, V. Veljkoviĉ, D. Skala, Assessment of $CaTiO_3$, $CaMnO_3$, $CaZrO_3$ and $Ca_2Fe_2O_3$ perovskites as heterogeneous base catalysts for biodiesel synthesis, Fuel Process. Technol 143 (2016) 162–168.
[27] A. Kawashima, K. Matsubara, K. Honda, Development of heterogeneous base catalysts for biodiesel production, Bioresour. Technol 99 (2008) 3439–3443.
[28] M. Li, X.L. Chen, D.F. Zhang, W.Y. Wang, W.J. Wang, Humidity sensitive properties of pure and Mg-doped $CaCu_3Ti_4O_{12}$, Sens. Actuators, B: Chem 147 (2010) 447–452.
[29] A. Sen, K.K. Chattopadhyay, Nanostructured $CaCu_3Ti_4O_{12}$ for environmental remediation through visible light active catalysis, J Mater Sci: Mater Electron 27 (2016) 10393–10398.
[30] M.S.A. Serafini, D.M. Reinoso, G.M. Tonetto, Response surface study and kinetic modelling of biodiesel synthesis catalyzed by zinc stearate, Energy 164 (2018) 264–274.
[31] A. Anwar, A. Garforth, Challenges and opportunities of enhancing cold flow properties of biodiesel via heterogeneous catalysis, Fuel 173 (2016) 189–208.
[32] S.N. Gebremariam, J.M. Marchetti, Techno-economic feasibility of producing biodiesel from acidic oil using sulfuric acid and calcium oxide as catalysts, Energ. Conver. Management 171 (2018) 1712–1720.
[33] K.A. Borges, A.L. Squissato, D.Q. Santos, W.B. Neto, A.C.F. Batista, T.A. Silva, A.T. Vieira, M.F. de Oliveira, M.G. Hernández-Terrones, Homogeneous catalysis of soybean oil transesterification via methylic and ethylic routes: Multivariate comparison, Energy 67 (2014) 569–574.
[34] A.E. Atabani, A.S. Silitonga, I.A. Badruddin, T.M.I. Mahlia, H.H. Masjuki, S. Mekhilef, A comprehensive review on biodiesel as an alternative energy resource and its characteristics, Renew Sust. Energy Rev. 16 (2012) 2070–2093.

[35] A. Shys, H. Nhm, A. Azid, R. Umar, H. Juahir, H. Khatoon, et al., A review of biomass-derived heterogeneous catalyst for a sustainable biodiesel production, Renew Sust Energy Rev. 70 (2017) 1040–1051.

[36] M. Kouzu, A. Fujimori, T. Suzuki, K. Koshi, H. Moriyasu, Industrial feasibility of powdery CaO catalyst for production of biodiesel, Fuel Process Technol. 165 (2017) 94–101.

[37] R. Madhuvilakku, S. Piraman, Biodiesel synthesis by TiO_2–ZnO mixed oxide nanocatalyst catalyzed palm oil transesterification process, Bioresour. Technol. 150 (2013) 55–59.

[38] M.C. Hsiao, C.C. Lin, Y.H. Chang, Microwave irradiation–assisted transesterification of soybean oil to biodiesel catalyzed by nanopowder calcium oxide, Fuel 90 (2011) 1963–1967.

[39] M. Raghavendra, K.V. Yatish, H.S. Lalithamba, Plant-mediated green synthesis of ZnO nanoparticles using Garcinia gummi-gutta seed extract: photoluminescence, screening of their catalytic activity in antioxidant, formylation and biodiesel production, Eur. Phys. J. Plus 132 (2017) 358.

[40] G. Baskar, M. Soumiya, Production of biodiesel from castor oil using iron (II) doped zinc oxide nanocatalyst, Renew. Energy 98 (2016) 101–107.

[41] G. Nagaraju, S.A. Prashanth, M. Shastri, K.V. Yathish, C. Anupama, D. Rangappa, Electrochemical heavy metal detection, Photocatalytic, Photoluminescence, Biodiesel production and Antibacterial activities of Ag-ZnO nanomaterial, Mater. Res. Bull. 94 (2017) 54–63.

[42] E.A. Faria, J.S. Marques, I.M. Dias, R.D.A. Andrade, P.A.Z. Suareza, A.G.S. Prado, Nanosized and reusable SiO_2/ZrO_2 catalyst for highly efficient biodiesel production by soybean transesterification, J. Braz. Chem. Soc. 20 (2009) 1732–1737.

[43] J. Matos, A. García, S.-E. Park, Ti-containing mesoporous silica for methylene blue photodegradation, Appl. Catal. A: General 393 (2011) 359–366.

[44] M. Darroudi, A. Zak, M.R. Muhamad, N.M. Huang, M. Hakimi, Green synthesis of colloidal silver nanoparticles by sonochemical method, Mater. Lett. 66 (2012) 117–120.

[45] X. Wu, Q. Jiang, Z. Ma, M. Fu, W. Shangguan, Synthesis of titania nanotubes by microwave irradiation, Solid State Commun. 136 (2005) 513–517.

[46] T. Touqeer, M.W. Mumtaz, H. Mukhtar, A. Irfan, S. Akram, A. Shabbir, U. Rashid, I.A Nehdi, T.S.Y. Choong, Fe3O4-PDA-Lipase as Surface Functionalized Nano Biocatalyst for the Production of Biodiesel Using Waste Cooking Oil as Feedstock: Characterization and Process Optimization, Energies 13 (2020) 177.

[47] M.B. Navas, J.F. Ruggera, I.D. Lick, M.L. Casella, A sustainable process for biodiesel production using Zn/Mg oxidic species as active, selective and reusable heterogeneous catalysts, Bioresour. Bioprocess. 7 (2020) 4.

[48] T. Wongwuttanasatiana, K. Jookjantra, Effect of dual-frequency pulsed ultrasonic excitation and catalyst size for biodiesel production, Renewable Energy 152 (2020) 1220–1226.

[49] R.M. Ali, M.R. Elkatory, H.A. Hamad, Highly active and stable magnetically recyclable $CuFe_2O4$ as a heterogenous catalyst for efficient conversion of waste frying oil to biodiesel, Fuel 268 (15) (2020), 117297.

[50] A. De, S.S. Boxi, Application of Cu impregnated TiO2 as a heterogeneous nanocatalyst for the production of biodiesel from palm oil, Fuel 265 (2020).

[51] Y.J. Wong, J. Hassan, M. Hashim, Dielectric properties, impedance analysis and modulus behavior of $CaTiO_3$ ceramic prepared by solid state reaction, J. Alloys Compd 571 (2013) 138–144.

[52] T.A. Plutenko, O.I. V'yunov, A.G. Belous, Synthesis and electrical properties of $(BaTiO_3)_{1-x}(K_{0.5}Bi_{0.5}TiO_3)_x$ solid solutions, Inorg. Mater 48 (2012) 1183–1189.

[53] M.R. Mohammadi, D.J. Fray, Synthesis of highly pure nanocrystalline and mesoporous $CaTiO_3$ by a particulate sol–gel route at the low temperature, J Sol-Gel Sci Technol 68 (2013) 324–333.

[54] K.P. Lopes, L.S. Cavalcante, A.Z. Simões, J.A. Varela, E. Longo, E.R. Leite, $NiTiO_3$ powders obtained by polymeric precursor method: Synthesis and characterization, J. Alloys Compd 468 (2009) 327–332.

[55] B.W. Lee, S.B. Cho, Hydrothermal preparation and characterization of ultra-fine $BaTiO_3$powders from amorphous peroxo-hydroxide precursor, J. Electroceram 13 (2004) 379–384.

[56] E. Djurado, E. Meunier, Synthesis of doped and undoped nanopowders of tetragonal polycrystalline zirconia (TPZ) by spray-pyrolysis, J. Solid. State Chem 141 (1998) 191–198.

[57] P. Vernoux, E. Djurado, M. Guillodo, Catalytic and electrochemical properties of doped lanthanum chromites as new anode materials for solid oxide fuel cells, J. Am. Ceram. Soc. 84 (2001) 2289–2295.

[58] D. Mesguich, J.-M. Bassat, C. Aymonier, A. Brüll, L. Dessemond, E. Djurado, Influence of crystallinity and particle size on the electrochemical properties of spray pyrolyzed $Nd_2NiO_{4+\delta}$ powders, Electrochim. Acta 87 (2013) 330–335.

[59] S. Lanfredi, F. Storti, L.P.M. Simões, E. Djurado, M.A.L. Nobre, Synthesis and structural characterization of calcium titanate by spray pyrolysis method, Mater. Lett. 201 (2017) 148–151.

[60] P.A. Stuart, T. Unno, R. Ayres-Rocha, E. Djurado, S.J. Skinner, The synthesis and sintering behaviour of $BaZr_{0.9}Y_{0.1}O_{3-\delta}$ powders prepared by spray pyrolysis, J. Eur., Ceram. Soc. 29 (2009) 697–702.

[61] C. Goulart, E. Djurado, Synthesis and sintering of Gd-doped CeO_2 nanopowders prepared by ultrasonic spray pyrolysis, J. Eur. Ceram. Soc 33 (2013) 769–778.

[62] K. Tanabe, M. Misono, Y. Ono, H. Hattori, New solid acids and bases, Kodansha, Tokyo and Elsevier, Amsterdam 51 (1989) 247–254.

[63] JADE 8 PLUS, XRD Pattern Processing and Identification Program, Materials Data, Inc. (1995-2007).

[64] J.R. Carvajal, An introduction to the Program FullProff 2000, CEA/Saclay, France, 2008.

[65] S. Lanfredi, C. Darie, F.S. Bellucci, C.V. Colin, M.A.L. Nobre, Phase transitions and interface phenomena at cryogenic temperature domain of a niobate nanostructured ceramic, Dalton Trans 43 (2014) 10983–10998.

[66] G. Caglioti, A. Paoletti, F.P. Ricci, Choice of collimators for crystal spectrometers

[67] E.R.P. González, Processo de obtenção de biodiesel utilizando oleo fúsel. BR1020180712705, issued October 16, 2018.

[68] G. Teng, L. Gao, G. Xiao, H. Liu, Transesterification of soybean oil to biodiesel over heterogeneous solid base catalyst, Energy & Fuels 23 (2009) 4630–4634.

[69] X. Liu, X. Piao, Y. Wang, S. Zhu, Calcium ethoxide as a solid base catalyst for the transesterification of soybean oil to biodiesel, Energy & Fuels 22 (2008) 1313–1317.

[70] C. Silva, T.A. Weschenfelder, S. Rovani, F.C. Corazza, M.L. Corazza, C. Dariva, J.V. Oliveira, Continuous production of fatty acid ethyl esters from soybean oil in compressed ethanol, Ind. Eng. Chem. Res. 46 (2007) 5304–5309.

[71] G.L. Messing, S.C. Zhang, G.V. Jayanthi, Ceramic powder synthesis by spray pyrolysis, J. Am. Ceram. Soc. 76 (1993) 2707–2726.

[72] M. Iida, T. Sasaki, M. Watanabe, Titanium dioxide hollow microspheres with an extremely thin shell, Chem. Mater. 10 (1998) 3780–3782.

[73] J. Matos, J. Ocares-Riquelme, P.S. Poon, R. Montaña, X. García, K. Campos, J.C. Hernández-Garrido, M.M. Titirici, C-doped anatase TiO_2: Adsorption kinetics and photocatalytic degradation of methylene blue and phenol, and correlations with DFT estimations, J. Colloid Interf. Sci. 547 (2019) 14–29.

[74] T.A.H. Nguyen, S. Biggs, A. Doi, A.V. Nguyen, A new way of assessing droplet evaporation independently of the substrate hydrophobicity and contact line mode: A case study of sessile droplets with surfactants, Coll. Surf. A: Physicochem. Eng. Aspects 577 (2019) 396–404.

[75] I. Lawan, Z.N. Garba, W. Zhou, M. Zhang, Z. Yuan, Synergies between the microwave reactor and CaO/zeolite catalyst in waste lard biodiesel production, Renew. Energy 145 (2020) 2550–2560.

[76] M. Thommes, K. Kaneko, A.V. Neimark, J.P. Olivier, F. Rodriguez-Reinoso, J. Rouquerol, K.S.W. Sing, Physisorption of gases, with special reference to the evaluation of surface area and pore size distribution (IUPAC Technical Report), Pure Appl. Chem 87 (2015) 1051–1069.

[77] A.F.L. Almeida, R.S. de Oliveira, J.C. Góes, J.M. Sasaki, A.G. Souza Filho, J. Mendes Filho, A.S.B. Sombra, Structural properties of $CaCu_3Ti_4O_{12}$ obtained by mechanical alloying, Mater. Sci. Eng. B. 96 (2002) 275–283.

[78] C.L. Kretly, A.F.L. Almeida, P.B.A. Fechine, R.S. de Oliveira, A.S.B. Sombra, Dielectric permittivity and loss of $CaCu_3Ti_4O_{12}$ (CCTO) substrates for microwave devices and antennas, J. Mater. Sci.: Mater. Electronics 15 (2004) 657–663.

[79] X. Jin, D. Sun, M. Zhang, Y. Zhu, J. Qian, Investigation on FTIR spectra of barium calcium titanate ceramics, J. Electroceram 22 (2009) 285–290.

[80] F. Gao, R.A. Lewis, X.L. Wang, S.X. Dou, Far-infrared reflection and transmission of $La_{1-x}Ca_xMnO_3$, J. Alloys Compd 347 (2002) 314–318.

[81] H.K. Yang, J.W. Chung, G.S.R. Raju, B.K. Moon, B.C. Choi, J.H. Jeong, J.H. Kim, Luminescent characteristics of $CaTiO_3:Pr^{3+}$ thin films prepared by pulsed laser deposition method with various substrates, Appl. Surf. Sci. 255 (2009) 5062–5066.

[82] W. Dua, W. Si, F. Wang, L. Lv, L. Wu, Z. Wang, J. Liu, W. Liu, Creating oxygen vacancies on porous indium oxide nanospheres via metallic aluminum reduction for enhanced nitrogen dioxide detection at low temperature, Sens. Actuators B: Chem. 303 (2020), 127221.

[83] I.R. Evans, J.A.K. Howard, T. Sreckovic, M.M. Ristic, Variable temperature in situ X-ray diffraction study of mechanically activated synthesis of calcium titanate, $CaTiO_3$, Mater. Res. Bull. 38 (2003) 1203–1213.

[84] M. Sindhu, N. Ahlawat, S. Sanghi, A. Agarwal, R. Dahiya, N. Ahlawat, Rietveld refinement and impedance spectroscopy of calcium titanate, Curr. Appl. Phys. 12 (2012) 1429–1435.

[85] S. Sahoo, U. Dash, S.K.S. Parashar, S.M. Ali, Frequency and temperature dependent electrical characteristics of $CaTiO_3$ nano-ceramic prepared by high-energy ball milling, J. Adv. Ceram. 2 (2013) 291–300.

[86] M. Muthuraman, K.C. Patil, S. Senbagaraman, A.M. Umarji, Sintering, microstructural and dilatometric studies of combustion synthesized synroc phases, Mater. Res. Bull 31 (1996) 1375–1381.

[87] P. Ctibor, J. Sedlacek, Selected aspects of dielectric behavior of plasma sprayed titanates, J. Adv. Ceram 1 (2012) 50–59.

[88] G.S. Nascimento, G.P. Mambrini, E.C. Paris, J.A. Peres, L.A. Colnago, C. Ribeiro, Evaluation of the catalytic activity of oxide nanoparticles synthesized by the polymeric precursor method on biodiesel production, J. Mater. Res. 27 (2012) 3020–3026.

[89] L.S. Cavalcante, V.S. Marques, J.C. Sczancoski, M.T. Escote, M.R. Joya, J.A. Varela, M.R.M.C. Santos, P.S. Pizani, E. Longo, Synthesis, structural refinement and optical behavior of $CaTiO_3$ powders: A comparative study of processing in different furnaces, Chem. Eng. J. 143 (2008) 299–307.

[90] G. Pfaff, Synthesis of calcium titanate powders by the sol-gel process, Chem. Mater 6 (1994) 58–62.

[91] P.K. Mallik, G. Biswal, S.C. Patnaik, S.K. Senapati, Characterization of sol-gel synthesis of phase pure $CaTiO_3$ nano powders after drying, Mater. Sci. Eng 75 (2015), 012005.

[92] S.C. Pereira, A.T. Figueiredo, C.M. Barrado, M.H. Stoppa, Y. Dwivedi, M.S. Li, E. Longo, Facile microwave-assisted synthesis of lanthanide doped $CaTiO_3$nanocrystals, J. Braz., Chem. Soc. 26 (2015) 2339–2345.

[93] M.L. Moreira, E.C. Paris, G.S. Nascimento, V.M. Longo, J.R. Sambrano, V.R. Mastelaro, M.I.B. Bernardi, J. Andre's, J.A. Varela, E. Longo, Structural and optical properties of $CaTiO_3$ perovskite-based materials obtained by microwave-assisted hydrothermal synthesis: An experimental and theoretical insight, Acta Mater 57 (2009) 5174–5185.

[94] T. Kimijima, K. Kanie, M. Nakaya, A. Muramatsu, Hydrothermal synthesis of size- and shape-controlled $CaTiO_3$ fine particles and their photocatalytic activity,, CrystEngComm. 16 (2014) 5591–5597.

[95] T.R.N. Kutty, R. Vivekanandan, P. Murugaraj, Precipitation of rutile and anatase (TiO_2) fine powders and their conversion to $MTiO_3$ (M = Ba, Sr, Ca) by the hydrothermal method, Mater. Chem. Phys 19 (1988) 533–546.

and hollow submicrospheres for photocatalytic oxygen evolution and mesoscopic solar cells, Appl. Mater. Interfaces 7 (2015) 14859–14869.

[97] H. Zhao, Y. Duan, X. Sun, Synthesis and characterization of $CaTiO_3$ particles with controlled shape and size, New J. Chem 37 (2013) 986–991.

[98] Y.S. Huo, H. Yang, T. Xian, J.L. Jiang, Z.Q. Wei, R.S. Li, W.J. Feng, A polyacrylamide gel route to different-sized $CaTiO_3$ nanoparticles and their photocatalytic activity for dye degradation, J. Sol-Gel Sci. Technol 71 (2014) 254–259.

[99] E.S. Kim, C.J. Jeon, Microwave dielectric properties of $ATiO_3$ (A = Ni, Mg, Co, Mn) ceramics, J. Eur. Ceram. Soc. 30 (2010) 341–346.

[100] R.D. Shannon, Revised effective ionic radii and systematic studies of interatomic distances in halides and chalcogenides, Acta Cryst. A 32 (1976) 751–767.

[101] R.B. Ljupković, R.D. Mićić, M.D. Tomić, N.S. Radulović, A. Bojić, A.R. Lj Zarubica, Significance of the structural properties of CaO catalyst in the production of biodiesel: An effect on the reduction of greenhouse gas emissions, Hem. Ind 68 (2014) 399–412.

[102] C.L. Marchena, C. Saux, R. Dinamarca, G. Pecchi, L. Pierella, Alkaline niobates $ANbO_3$ (A = Li, Na, K) as heterogeneous catalysts for dipropyl sulfide oxidation, RSC Adv 6 (2016) 102015–102022.

[103] K. Yang, Y. Zhang, Y. Li, P. Huang, X. Chen, W. Dai, X. Fu, Insight into the function of alkaline earth metal oxides as electron promoters for Au/TiO_2 catalysts used in CO oxidation, Appl. Catal. B 183 (2016) 206–215.

[104] J. Matos, M. Rosales, R. Demir-Cakan, M.M. Titirici, Methane conversion on Pt-Ru nanoparticles alloy supported on hydrothermal carbon, Appl. Catal. A: Gen. 386 (2010) 140–146.

[105] B.Y. Kim, J.W. Yoon, K. Lim, S.H. Park, J.W. Yoon, J.H. Lee, Hollow spheres of $CoCr_2O_4$–Cr_2O_3 mixed oxides with nanoscale heterojunctions for exclusive detection of indoor xylene, J. Mater. Chem. C 6 (2018) 10767–10774.

[106] A.Z. Abdullah, N. Razali, K.T. Lee, Optimization of mesoporous K/SBA-15 catalyzed transesterification of palm oil using response surface methodology, Fuel Proc. Technol. 90 (2009) 58–964.

[107] B. Al-Shammari, Q.A. Alsulami, K. Narasimharao, Lanthanum exchanged Keggin structured heteropoly compounds for biodiesel production, Catalysts 9 (2019) 979.

[108] J.C.M. da Silva, C.L. Nicolau, M.R.P. Cabral, E.R. Costa, J.M. Stropa, C.A.A. Silva, D.R. Scharf, E.L. Simionatto, A.R. Fiorucci, L.C.S. de Oliveira, E. Simionatto, Thermal and oxidative stabilities of binary blends of esters from soybean oil and non-edible oils (Aleurites moluccanus, Terminalia catappa, and Scheelea phalerata), Fuel 262 (2020), 116644.

[109] C.V.P. Pascoal, A.L.L. Oliveira, D.D. Figueiredo, J.C.C. Assunção, Optimization and kinetic study of ultrasonic-mediated in situ transesterification for biodiesel production from the almonds of Syagrus cearensis, Renew. Energy 147 (2020) 1815–1824.

[110] H.-S. Lee, H. Seo, D. Kim, Y.-W. Lee, One-pot supercritical transesterification and partial hydrogenation of soybean oil in the presence of Pd/Al_2O_3 or Cu or Ni catalyst without H_2, J. Supercritical Fluids 156 (2020), 104683.

[111] A. Sharma, P. Kodgire, S.S. Kachhwaha, Investigation of ultrasound-assisted KOH and CaO catalyzed transesterification for biodiesel production from waste cotton-seed cooking oil: Process optimization and conversion rate evaluation, J. Cleaner Prod. 259 (2020), 120982.

[112] M. Unglert, D. Bockey, C. Bofinger, B. Buchholz, G. Fisch, R. Luther, M. Müller, K. Schaper, J. Schmitt, O. Schröder, U. Schümann, H. Tschöke, E. Remmele, R. Wicht, M. Winkler, J. Krahl, Action areas and the need for research in biofuels, Fuel 268 (2020), 117227.

[113] E. Alptekin, M. Canakci, Determination of the density and the viscosities of biodiesel-diesel fuel blend, Renewable Energy 12 (2008) 2623–2630.

[114] L. Meher, D. Vidya Sagar, S. Naik, Technical aspects of biodiesel production by transesterification- a review, Renewable and Sustainable Energy Reviews 10 (2006) 248–268.

[115] J.B. Heywood, Internal combustion engine fundamentals, McGraw- Hill. New York, 1988.

[116] M. Tate, J. Garpen, The specific gravity of biodiesel and its blends with diesel fuel, J. Am. Oil Chem. Soc. 77 (2000) 115–119.